



Elastic immersive wavefield modelling

Xun Li^{a,*}, Erik Koene^a, Dirk-Jan van Manen^a, Johan Robertsson^a, Andrew Curtis^b

^a Institute of Geophysics, ETH Zurich, Sonneggstrasse 5, 8092 Zurich, Switzerland

^b School of GeoSciences, University of Edinburgh, James Hutton Road, Edinburgh EH9 3FE, UK



ARTICLE INFO

Article history:

Available online 9 November 2021

Keywords:

Numerical methods
Local-domain modelling
Immersive boundary condition
Boundary integral equation
Unbounded domain
Wave scattering and diffraction

ABSTRACT

Many modelling studies of wave scattering require repeated numerical simulations through models with properties that differ only in a small sub-domain. Hence, it is of interest to recompute the wavefields that account for wave propagation through the whole domain, using simulations that are performed only in the sub-domain. Immersive boundary conditions (IBCs) can be used to establish such a local wavefield modelling scheme which enables accurate wavefield recomputation, including all interactions between the locally-perturbed medium and the full domain. We develop IBC theory for elastic wave propagation, in which the boundary conditions are updated dynamically at each time step of a simulation in the local domain. These updates are calculated by wavefield extrapolation based on the Kirchhoff-Helmholtz integrals using Green's functions in the background medium. Wavefield recording and injection in IBCs can be implemented either using finite-difference (FD) injection methods, or using the method of multiple point sources (MPS). The latter method is significantly less computationally demanding in terms of both memory and number of calculations. We therefore both extend acoustic FD injection methods to elastic media, and propose a new second-order accurate MPS method to implement elastic IBCs, which is numerically exact. In higher-order FD modelling, the MPS method is not numerically exact but still produces highly accurate IBC wavefields when compared to global-domain simulations.

© 2021 The Author(s). Published by Elsevier Inc. This is an open access article under the CC BY license (<http://creativecommons.org/licenses/by/4.0/>).

1. Introduction

Many numerical studies such as full waveform inversion (FWI) [e.g., 12,55,67] and the design of wave-based imaging and monitoring surveys [e.g., 36,49,52] require wave simulations for a suite of closely related models. In these applications, model changes may be restricted to small sub-domains within the global model, in which case it is not computationally attractive to perform the simulations on the full model to recompute seismic responses after those changes. Recomputing the full wavefield while performing only local wavefield simulations on a sub-domain that encloses the model alterations would significantly reduce the required computational resources, so this has been an active area of research in exploration geophysics and seismology [e.g., 1,22,28,42]. Local-domain modelling can also be applied for investigating a target of interest inside a sub-volume of a medium, for example, in nondestructive testing where damage zones are commonly highly localised [e.g., fracture corridors, see Refs. 41,71,73], in medical acoustics where modelling targets are often local organs such

* Corresponding author.

E-mail address: lixunjack@gmail.com (X. Li).

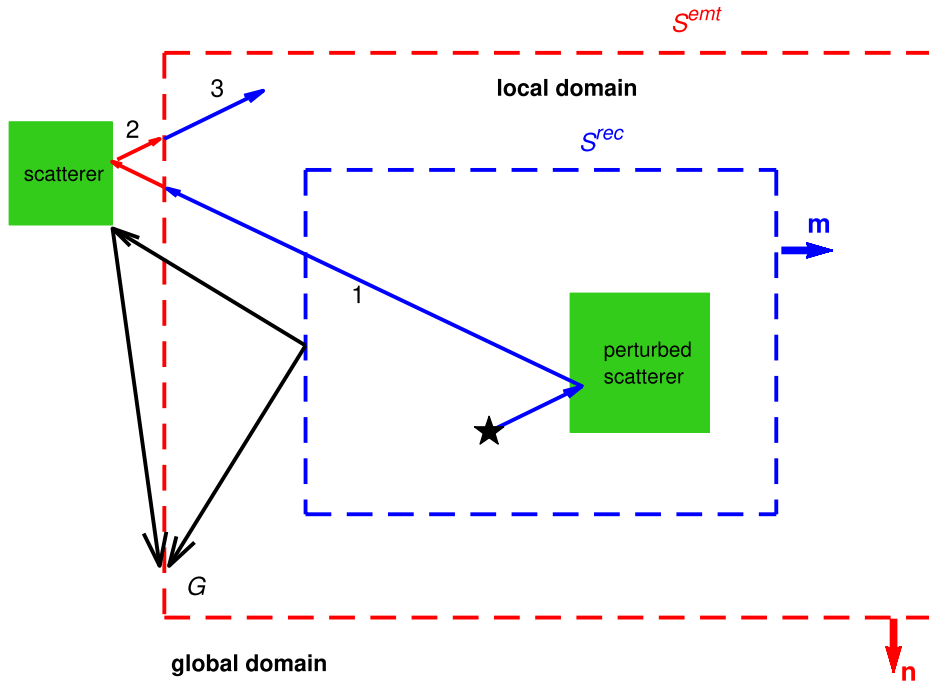


Fig. 1. (Colour online) Schematic plot of immersive boundary conditions (IBCs). The dashed red rectangle (S^{emt}) represents the boundary of a local domain, while the dashed blue rectangle represents the recording surface S^{rec} . The black star denotes a source that generates wave energy in an IBC simulation. Arrows 1 to 3 show paths of wave propagation explicitly in the sub-domain and implicitly outside. Black arrows denote the pre-computed Green's functions connecting receivers on S^{rec} and sources on S^{emt} .

as a beating artery or liver fat [e.g., 25,44,54], and in modelling of electromagnetic waves such as for ground-penetrating radar (GPR) which are often used to detect a local target in the Earth's subsurface [3,21,26]. Particularly for imaging and inversion in all of these fields [e.g., 5,10,19,32,40,68], local-domain simulations may be useful to save computational cost compared to simulating full models.

The conventional approach for such local wavefield recomputation involves a simulation on the full model during which the wavefield quantities are recorded around a user-defined surface. Then in a second simulation the modelled material properties may be altered within that surface and the recorded wavefield quantities are injected around the surface; this reproduces the local wavefield *only* inside that enclosed sub-domain, which can then be extrapolated to the rest of the domain using a variety of techniques [e.g., 33,47]. However, this strategy cannot correctly compute so-called higher-order long-range interactions between the local and exterior domains due to the local model alterations.

van Manen et al. [31] and Vasmel et al. [64] propose so-called immersive boundary conditions (IBCs) that allow the local wavefield to be recomputed by simulating only the sub-domain, while maintaining full interaction with the rest of the medium. They implemented IBC-based local-domain modelling for acoustic or scalar media, and these IBCs have since been applied to acoustic full waveform inversion [e.g., 11,72] and localised tomography [e.g., 35]. In this paper, we further develop IBC theory to allow full wavefield simulations to be obtained from local wavefield modelling in elastic media.

Any IBC simulation is performed in a local modelling domain in which two surfaces exist as shown in Fig. 1: an outer emitting boundary S^{emt} with sources enclosing the simulated local domain, and an inner recording surface S^{rec} spanned by receivers. In IBC simulations, the emitting boundary S^{emt} absorbs outgoing waves (ray path 1 in Fig. 1) and generates the ingoing waves that correspond to the interaction between the local and global domains (ray path 3). This interaction is controlled by sources on S^{emt} whose signatures are calculated by means of Kirchhoff-Helmholtz integrals that extrapolate wavefields measured on S^{rec} to S^{emt} . The wavefield extrapolation relies on pre-computed Green's functions, generated in the full, unperturbed model before carrying out the IBC simulation. In IBC simulations, the Kirchhoff-Helmholtz integrals are evaluated at every time step to update the boundary condition on S^{emt} : waves propagating in the global domain (ray path 2 in Fig. 1) are therefore not explicitly modelled, but are included implicitly in the boundary conditions. In the general IBC methodology introduced above, the emitting boundary S^{emt} , as shown in Fig. 1, is a transparent boundary on which source injection takes place. A common practice, as used in acoustic IBCs, involves setting up a numerical reflecting boundary condition (i.e., a free surface¹ or rigid boundary²) on S^{emt} when carrying out an IBC simulation inside S^{emt} [e.g., 9,64].

¹ I.e., the surface where normal tractions are kept zero.

² I.e., the surface where normal particle displacement or velocity is kept zero.

This practice allows to further save computational and memory storage cost in acoustic local-domain simulations [e.g., 63], and is useful for simulating IBC-based physical laboratory experiments such as immersive wave experimentation that allows the immersion of a physical experiment into an arbitrary numerical environment [6,7,27,59]. However in elastic IBCs used for local-domain modelling, we focus only on the transmitting boundary condition case for S^{emt} (i.e., a non-reflecting, transparent boundary) since the current implementations of elastic free surfaces and rigid boundaries are not as accurate as their acoustic counterparts in finite-difference (FD) modelling [24,38,39,46].

Important ingredients for implementing immersive wavefield modelling are the wavefield recording and injection methods used to carry out source injection on the emitting boundary S^{emt} , and the wavefield extrapolation required to implement IBCs. The accuracy of local-domain modelling involves comparing a locally-computed wavefield and a counterpart global-domain simulation; ideally the two wavefields that are computed locally and globally should exactly match each other with a numerical difference as low as machine calculations allow. For elastic wavefield recording and injection, Mittet [37] proposed a method of multiple point sources (MPS) for FD modelling involving staggered stress and particle acceleration grids. Koene and Robertsson [23] and Aaker et al. [1] further extend this MPS method for the widely-used velocity-stress FD scheme [65]. However, while MPS can be used to implement IBCs accurately to machine precision in acoustic media [e.g., 63], existing methods such as the MPS method introduced by Mittet [37], do not produce locally-computed wavefields that are numerically exact.

In this paper, we propose a new method to implement wavefield recording and injection using MPS in elastic IBCs for velocity-stress FD modelling. We demonstrate that elastic IBCs can be implemented using this method with machine-precision accuracy for second-order (in both time and space) FD modelling, and that high accuracy is maintained in a higher-order (in space) FD scheme. We also implement elastic IBCs with FD injection - a different technique for wavefield recording and injection that is accurate to machine precision [e.g., 47]. However, using MPS for IBCs saves a significant amount of computational power and memory compared to using FD injection, especially in higher-order FD modelling, and for multi-component wavefields such as those simulated in elastic media.

In Section 2, we introduce elastic IBC theory and present the new method of MPS to implement the theory for IBC simulations. In Section 3, we show numerical examples of IBCs. In Section 4, we discuss (a) the accuracy of MPS, (b) the computational and memory storage cost of IBC simulations and (c) the possibility of collocating recording and emitting surfaces in IBCs. Section 5 summarises our conclusions.

2. Method

2.1. Elastic immersive boundary conditions

Elastic wavefield propagation in a solid medium can be described by the stress tensor $\tau_{ij}(\mathbf{x}, t)$ and particle velocity $v_i(\mathbf{x}, t)$ governed by the equation of motion [65]:

$$\rho(\mathbf{x}) \frac{\partial v_i(\mathbf{x}, t)}{\partial t} = \frac{\partial \tau_{ij}(\mathbf{x}, t)}{\partial x_j} + f_i(\mathbf{x}, t) \quad (1)$$

where t is time, \mathbf{x} represents a Cartesian coordinate, $\rho(\mathbf{x})$ is mass density, and $f_i(\mathbf{x}, t)$ denotes a distribution of body force (density) sources. Einstein's summation applies to repeated subscripts in this paper. The stress-strain relation is:

$$\frac{\partial \tau_{ij}(\mathbf{x}, t)}{\partial t} = c_{ijkl}(\mathbf{x}) \frac{\partial v_l(\mathbf{x}, t)}{\partial x_k} + c_{ijkl}(\mathbf{x}) h_{kl}(\mathbf{x}, t) \quad (2)$$

where c_{ijkl} is a fourth-rank stiffness tensor, and h_{kl} denotes a distribution of deformation rate (density) sources. An elastic representation theorem can be derived from Equations (1) and (2) (see Appendix A), and the surface integral of the derived theorem provides the effect of the immersive boundary condition:

$$v_n^{IBC}(\mathbf{x}, t) = \oint_{S^{emt}} (\tau_{ij}(\mathbf{x}_{emt}, t) * G_{n,i}^{v,f}(\mathbf{x}, t | \mathbf{x}_{emt}, 0) - v_i(\mathbf{x}_{emt}, t) * G_{n,ij}^{v,h}(\mathbf{x}, t | \mathbf{x}_{emt}, 0)) n_j dS(\mathbf{x}_{emt}) \quad (3)$$

This provides the basis for implementing sources on the emitting boundary or surface S^{emt} (Fig. 1). In Equation (3), $v_n^{IBC}(\mathbf{x}, t)$ is the particle velocity wavefield due to sources on S^{emt} , n_j is the outward-pointing normal vector component of S^{emt} , the symbol $*$ denotes temporal convolution, the Green's function $G_{n,i}^{v,f}(\mathbf{x}, t | \mathbf{x}_{emt}, 0)$ represents the particle velocity wavefield (superscript v) in the direction x_n (subscript n) recorded at the location \mathbf{x} due to an impulsive point source of body force (superscript f) in the x_i direction (subscript i) at \mathbf{x}_{emt} , and $G_{n,ij}^{v,h}(\mathbf{x}, t | \mathbf{x}_{emt}, 0)$ represents the particle velocity wavefield due to an impulsive point source of deformation rate (superscript h). The Green's functions G in Equation (3) are associated with the medium in the local domain of an IBC simulation; they are not recorded but act as the so-called propagators which propagate wavefields from the domain boundary S^{emt} into the local domain [43].

The right side of Equation (3) can be interpreted as an active boundary condition, with densely-spaced sources on the emitting surface S^{emt} enclosing a local domain (Fig. 1). The convolution term $\tau_{ij} n_j * G_{n,i}^{v,f}$ is interpreted as the effect inside

the local domain due to body force sources f_i (on S^{emt}) with normal tractions $\tau_{ij} n_j$ as the corresponding source signatures, and $v_i * G_{n,ij}^{v,h} n_j$ is interpreted as the effect inside the local domain due to normal deformation rate sources $h_{ij} n_j$ (on S^{emt}) with particle velocities v_i as the corresponding source signatures. In this scenario, the source terms f_i and h_{ij} (with subscript $kl \leftrightarrow ij$) in Equations (1) and (2) become:

$$f_i(\mathbf{x}, t) = \oint_{S^{emt}} \delta(\mathbf{x} - \mathbf{x}_{emt}) \tau_{ij}(\mathbf{x}_{emt}, t) n_j dS(\mathbf{x}_{emt}) + f'_i(\mathbf{x}, t) \quad (4)$$

and

$$h_{ij}(\mathbf{x}, t) = \oint_{S^{emt}} \delta(\mathbf{x} - \mathbf{x}_{emt}) v_i(\mathbf{x}_{emt}, t) n_j dS(\mathbf{x}_{emt}) + h'_{ij}(\mathbf{x}, t) \quad (5)$$

where $\delta(\cdot)$ denotes the Dirac distribution, and f'_i and h'_{ij} denote other sources *not* on S^{emt} (e.g., the black star in Fig. 1). Other examples of interpreting the surface integrals in representation theorems as boundary conditions can be found in Mittel [37] and Aki and Richards [2].

In Equations (4) and (5), both the stresses $\tau_{ij}(\mathbf{x}_{emt}, t)$ and particle velocities $v_i(\mathbf{x}_{emt}, t)$ are wavefield quantities that in theory should be obtained at the location of the emitting surface S^{emt} in the simulation on the full model including the medium perturbations in the sub-domain. Hence these quantities cannot be obtained directly on S^{emt} in an IBC simulation on a local domain [31]. Instead, $\tau_{ij}(\mathbf{x}_{emt}, t)$ and $v_i(\mathbf{x}_{emt}, t)$ can be obtained through wavefield extrapolation, using the following Kirchhoff-Helmholtz integrals based on the wavefields measured on a recording surface S^{rec} placed inside the local domain (see Fig. 1):

$$v_i(\mathbf{x}_{emt}, t) = \oint_{S^{rec}} \left(-\tau_{kl}(\mathbf{x}_{rec}, t) * \Gamma_{i,k}^{v,f}(\mathbf{x}_{emt}, t | \mathbf{x}_{rec}, 0) - v_k(\mathbf{x}_{rec}, t) * \Gamma_{i,kl}^{v,h}(\mathbf{x}_{emt}, t | \mathbf{x}_{rec}, 0) \right) m_l dS(\mathbf{x}_{rec}) \quad (6)$$

and

$$\tau_{ij}(\mathbf{x}_{emt}, t) = \oint_{S^{rec}} \left(-\tau_{kl}(\mathbf{x}_{rec}, t) * \Gamma_{ij,k}^{\tau,f}(\mathbf{x}_{emt}, t | \mathbf{x}_{rec}, 0) - v_k(\mathbf{x}_{rec}, t) * \Gamma_{ij,kl}^{\tau,h}(\mathbf{x}_{emt}, t | \mathbf{x}_{rec}, 0) \right) m_l dS(\mathbf{x}_{rec}) \quad (7)$$

where m_l is the normal vector component of S^{rec} , and the Green's functions Γ pertain to a global domain with an arbitrary structure inside S^{rec} . Derivations of the Kirchhoff-Helmholtz extrapolation integrals are given in Appendix B. Wavefield extrapolation using Kirchhoff-Helmholtz integrals allow medium properties (associated with Γ) inside S^{rec} to be changed arbitrarily in local-domain simulations since the (perturbed) medium inside S^{rec} is irrelevant to the derivation of Kirchhoff-Helmholtz integrals (see Appendix B). This property allows IBCs to correctly recompute the wavefield in a local domain as long as the regions of change are located inside a region enclosed by the recording surface S^{rec} [9], and the local and global models have identical material properties between S^{rec} and S^{emt} . In IBCs, the sources f'_i and h'_{ij} [in Equations (4) and (5)] can also be placed outside of S^{emt} but cannot be placed between S^{rec} and S^{emt} [see Ref. 9].

2.2. Velocity-stress finite-difference modelling

In this paper, we carry out immersive wavefield modelling using the velocity-stress finite-difference (FD) method which was proposed by Virieux [65] to simulate elastic wave propagation based on Equations (1) and (2) for a linear isotropic lossless medium (i.e., for elastodynamics). This FD method involves the velocity-stress staggered grid shown in Fig. 2(a), and the accuracy of the method can be simply denoted as $O(2, 2L)$ for second-order accuracy in time and $(2L)$ th-order accuracy in space. For an isotropic medium, the stiffness tensor c_{ijkl} in Equation (2) can be replaced by Lamé parameters λ and μ via

$$c_{ijkl}(\mathbf{x}) = \lambda(\mathbf{x}) \delta_{ij} \delta_{kl} + \mu(\mathbf{x}) (\delta_{ik} \delta_{jl} + \delta_{jk} \delta_{il})$$

where δ is Kronecker delta. The Lamé parameters λ and μ are related to compressional and shear wave velocities V_p and V_s via

$$V_p(\mathbf{x}) = \sqrt{\frac{\lambda(\mathbf{x}) + 2\mu(\mathbf{x})}{\rho(\mathbf{x})}}$$

and

$$V_s(\mathbf{x}) = \sqrt{\frac{\mu(\mathbf{x})}{\rho(\mathbf{x})}}$$

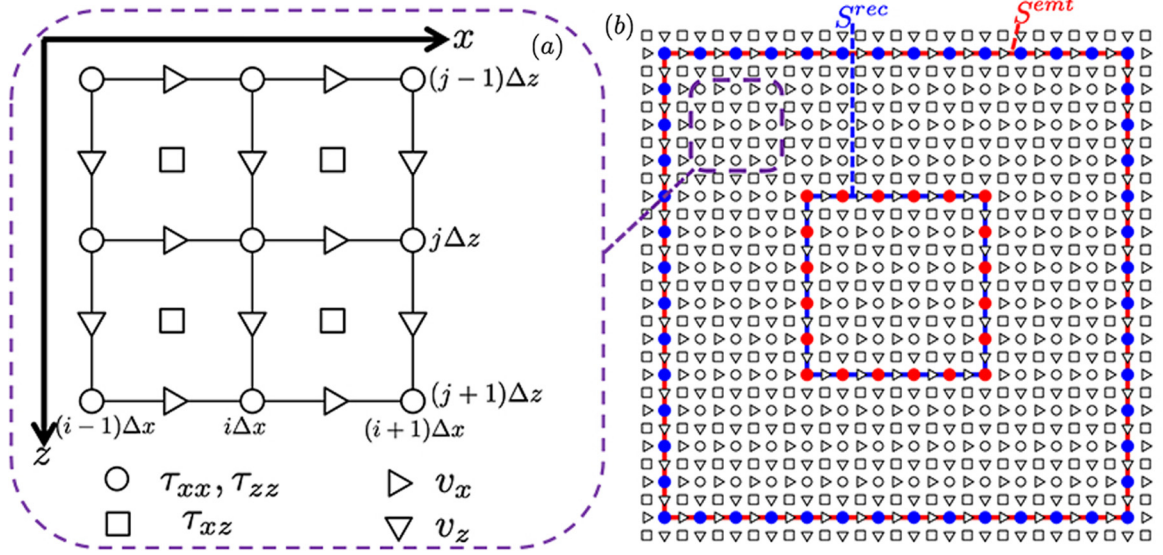


Fig. 2. (Colour online) (a) Staggered velocity-stress grids for FD simulations. The solid line denotes the main FD grid in Cartesian coordinate x, z , with grid sizes Δx and Δz . (b) The densely-spaced sources (blue dots) on the emitting surface S^{emt} (solid red line) and densely-spaced receivers or measurement points (red dots) on the recording surface S^{rec} (solid blue line).

2.3. Wavefield recording and injection methods

Since elastic wavefields are simulated using a staggered-grid FD method, recording and injecting a wavefield on a single layer or surface (e.g., for implementing S^{emt} and S^{rec} shown in Fig. 1) is challenging due to the staggered nature of FD quantities. Hence, special attention must be paid to wavefield recording and injection schemes for implementing local-domain simulations using IBCs. Hence, we propose a method of multiple point sources (MPS) which is designed for the 2D staggered-grid FD modelling method (with coordinates x, z); the extension to a 3D scheme should be straightforward.

2.3.1. MPS wavefield recording

In a 2D IBC simulation, the particle velocities $v_k(\mathbf{x}_{rec}, t)$ for Equations (6) and (7) are obtained on the recording surface S^{rec} at each FD time step of the simulation. The recording surface S^{rec} coincides with the main FD grid that runs through FD quantities τ_{xx} and τ_{zz} , as shown in Figs. 2(a) and (b), and the receivers or measurement points share the same locations with the nodes of τ_{xx} and τ_{zz} on S^{rec} . Note that obtaining all wavefield quantities exactly at the locations of these measurement points is desired, but in staggered-grid FD modelling, the values of measured FD wavefield quantities may need to be obtained from neighbouring staggered grids on which FD quantities are actually located.

The recording surface S^{rec} is composed of vertical (V) and horizontal (H) line segments with different unit normal vectors $\mathbf{m}^V = (\pm 1, 0)$ and $\mathbf{m}^H = (0, \pm 1)$ (± 1 for pointing to positive or negative direction along x or z axis). A recording of $v_x(\mathbf{x}_{rec})$ depends on whether the measurement point at $\mathbf{x}_{rec} = (i\Delta x, j\Delta z)$ [writing (i, j) as shortened notation in this paper] is located at a vertical line [i.e., $\mathbf{m}(\mathbf{x}_{rec}) = \mathbf{m}^V$ with \mathbf{m} as the normal of S^{rec}] or a horizontal line [i.e., $\mathbf{m}(\mathbf{x}_{rec}) = \mathbf{m}^H$]:

$$\bar{v}_x(\mathbf{x}_{rec}) = \begin{cases} \sum_{l=1}^L \alpha_l [v_x(i + 1/2 - l, j, t) + v_x(i - 1/2 + l, j, t)] & \text{for } \mathbf{m}(\mathbf{x}_{rec}) = \mathbf{m}^V \\ v_x(i + 1/2, j, t) & \text{for } \mathbf{m}(\mathbf{x}_{rec}) = \mathbf{m}^H \end{cases} \quad (8)$$

where the overbar symbol $\bar{\cdot}$ denotes the computed value of a wavefield quantity (i.e., v_x) at a measurement point $\mathbf{x}_{rec} = (i, j)$, and α_l are the interpolation coefficients with the (spatial) order of accuracy $2L$ [14], which should be consistent with the FD scheme used [63]. Recording $v_z(\mathbf{x}_{rec})$ follows similarly:

$$\bar{v}_z(\mathbf{x}_{rec}) = \begin{cases} v_z(i, j + 1/2, t) & \text{for } \mathbf{m}(\mathbf{x}_{rec}) = \mathbf{m}^V \\ \sum_{l=1}^L \alpha_l [v_z(i, j + 1/2 - l, t) + v_z(i, j - 1/2 + l, t)] & \text{for } \mathbf{m}(\mathbf{x}_{rec}) = \mathbf{m}^H \end{cases} \quad (9)$$

In order to record normal tractions $\tau_{kl}(\mathbf{x}_{rec}) m_l$ in Equations (6) and (7), $\bar{\tau}_{xx}$ and $\bar{\tau}_{zz}$ can be obtained directly at the locations of the measurement points that are coinciding with the nodes of τ_{xx} and τ_{zz} [see Fig. 2(b)]. For $\bar{\tau}_{xz}$ (where $\tau_{xz} = \tau_{zx}$), the recording scheme reads

$$\bar{\tau}_{xz}(\mathbf{x}_{rec}) = \begin{cases} \sum_{l=1}^L \alpha_l [\tau_{xz}(i+1/2-l, j+1/2), t) + \tau_{xz}(i-1/2+l, j+1/2, t)] & \text{for } \mathbf{n}(\mathbf{x}_{rec}) = \mathbf{m}^V \\ \sum_{l=1}^L \alpha_l [\tau_{xz}(i+1/2, j+1/2-l, t) + \tau_{xz}(i+1/2, j-1/2+l, t)] & \text{for } \mathbf{n}(\mathbf{x}_{rec}) = \mathbf{m}^H \end{cases} \quad (10)$$

Fig. 3 shows an example of the MPS recording scheme for O(2,2) FD modelling with second-order accuracy in both time and space. The recording schemes shown in Fig. 3 correspond to the cases where a measurement point is located at either the vertical line or the horizontal line around the upper left corner of the recording surface S^{rec} , and the situation for the other two lines (of S^{rec}) follows the same principle. The wavefield recording at sharp corners where normal direction(s) of S^{rec} [e.g., m_l in Equations (6) and (7)] cannot be defined will be discussed in Section 2.3.3. Another example of this MPS recording scheme for higher-order FD modelling [O(2,4) with fourth-order accuracy in space] is shown in Appendix C.

Note that our MPS scheme as presented calculates recordings at a single, common measurement point \mathbf{x}_{rec} on S^{rec} for all IBC-related FD wavefield quantities that are located on either the main or staggered FD grids. This is only for the purpose of concise notation. While wavefield quantities v_x and v_z should be recorded exactly on S^{rec} , the true array of receivers on S^{rec} are not represented by the grid locations of v_x and v_z exactly. In other words, the discretized, integer locations of the measurement points [i.e., (i, j)] can be different from the locations of actual MPS recording points. For example, the measurement point $\mathbf{x}_{rec} = (i, j)$ on the left side of Equation (8) does not share the same location with the corresponding actual recording point, indicated on the right side of Equation (8). For the measurement involving more than one wavefield quantity [e.g., the two solid black symbols in Fig. 3(a, left)], the MPS recording point is defined to be at the middle of the two wavefield quantities involved and should be located exactly on the same level of S^{rec} [63]. Also, we choose receivers or measurement points on S^{rec} to coincide with the nodes of τ_{xx} and τ_{zz} [see Fig. 2(b)] such that their values can be obtained directly at the locations of the measurement points, but other choices may also be feasible. Our MPS method is not limited by the placement of a recording surface S^{rec} coinciding with the main FD grid, and S^{rec} can also run through staggered v_x , v_z , and τ_{xz} grids, with the MPS wavefield recording scheme slightly modified according to a different staggered nature of FD quantities. A similar idea applies to MPS wavefield injection presented in the next section.

2.3.2. MPS wavefield injection

In IBC simulations on a local domain, wavefield injection by MPS applies to the implementation of the emitting surface S^{emt} (see Fig. 1). Here, we show only the source injection scheme, i.e., how $\delta(\mathbf{x} - \mathbf{x}_{emt})$ in Equations (4) and (5) is *actually* implemented for various types of sources in elastic FD modelling over the space-discrete and time-invariant grids. For the source signatures, i.e., wavefield quantities to be injected onto the FD grids, we refer to Equations (4) and (5) for the terms multiplied by $\delta(\cdot)$ functions.

In IBCs implemented with MPS, the emitting surface S^{emt} is placed so as to be coinciding with the main FD grid that runs through the nodes of normal stresses τ_{xx} and τ_{zz} , and sources are densely distributed on S^{emt} as shown in Fig. 2(b). The implementations of these sources on S^{emt} [with unit normal vectors $\mathbf{n}^V = (\pm 1, 0)$ and $\mathbf{n}^H = (0, \pm 1)$] depend on whether $\mathbf{x}_{emt} = (i, j)$ is at the vertical lines [$\mathbf{n}(\mathbf{x}_{emt}) = \mathbf{n}^V$ with \mathbf{n} as the normal of S^{emt}] or horizontal lines [$\mathbf{n}(\mathbf{x}_{emt}) = \mathbf{n}^H$] of S^{emt} . The sources f_x are implemented as:

$$\tilde{\delta}_{f_x}(\mathbf{x} - \mathbf{x}_{emt}) = \begin{cases} \sum_{l=1}^L \alpha_l [\delta(\mathbf{x} - \mathbf{x}_{-l}) + \delta(\mathbf{x} - \mathbf{x}_l)] \\ \text{where } \mathbf{x}_{-l} = (i+1/2-l, j) \text{ and } \mathbf{x}_l = (i-1/2+l, j) & \text{for } \mathbf{n}(\mathbf{x}_{emt}) = \mathbf{n}^V \\ \delta(\mathbf{x} - \mathbf{x}_0) \\ \text{where } \mathbf{x}_0 = (i+1/2, j) & \text{for } \mathbf{n}(\mathbf{x}_{emt}) = \mathbf{n}^H \end{cases} \quad (11)$$

where $\tilde{\delta}_{f_x}$ represents the FD approximation to the theoretically-required source f_x [see Equation (4)] in the subscript at $\mathbf{x}_{emt} = (i, j)$, and the symbol \sim denotes source injection that cannot be done directly in the FD grid (i, j) but can be done at neighbouring FD nodes (e.g., $\mathbf{x}_{\pm l}$ and \mathbf{x}_0). Similarly, the sources f_z are implemented as

$$\tilde{\delta}_{f_z}(\mathbf{x} - \mathbf{x}_{emt}) = \begin{cases} \delta(\mathbf{x} - \mathbf{x}_0) \\ \text{where } \mathbf{x}_0 = (i, j+1/2) & \text{for } \mathbf{n}(\mathbf{x}_{emt}) = \mathbf{n}^V \\ \sum_{l=1}^L \alpha_l [\delta(\mathbf{x} - \mathbf{x}_{-l}) + \delta(\mathbf{x} - \mathbf{x}_l)] \\ \text{where } \mathbf{x}_{-l} = (i, j+1/2-l) \text{ and } \mathbf{x}_l = (i, j-1/2+l) & \text{for } \mathbf{n}(\mathbf{x}_{emt}) = \mathbf{n}^H \end{cases} \quad (12)$$

The deformation rate sources h_{xx} and h_{zz} can be directly implemented as source injection on the FD nodes τ_{xx} and τ_{zz} , respectively. The deformation rate sources h_{xz} and h_{zx} ($h_{xz} \neq h_{zx}$) are implemented as:

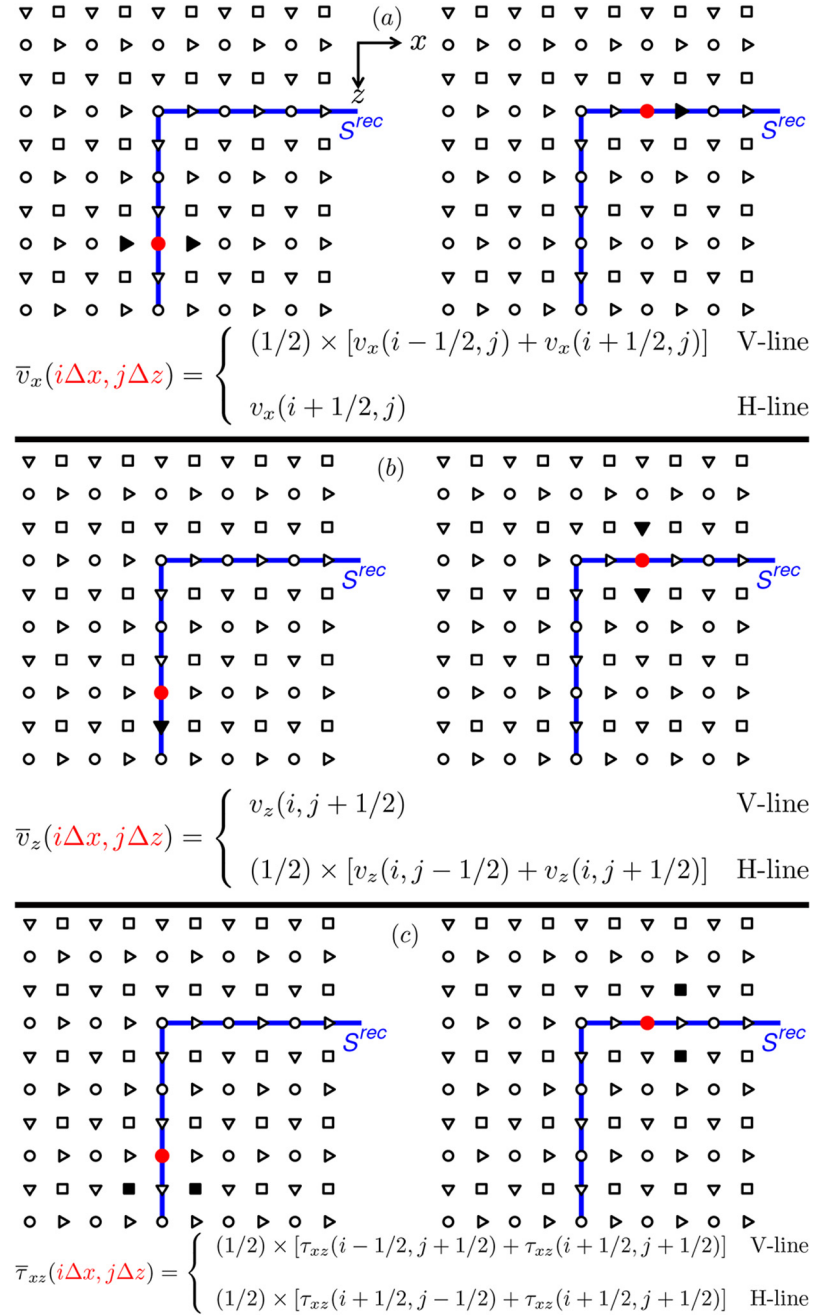


Fig. 3. (Colour online) MPS wavefield recording in the O(2,2) FD scheme (second-order accuracy in both time and space). (a) Recording of v_x for a measurement point (red dot) located on a vertical part (left plot) or a horizontal part (right plot) of S^{rec} . The solid black symbols denote the quantities involved for calculating actual recording in the staggered FD grid. The equations are associated with the two plots and are the same as Equation (8) with $L = 1$; 'V-line' denotes the case where the measurement point at $(i\Delta x, j\Delta z)$ is on a vertical part of S^{rec} and 'H-line' denotes the case where the measurement point is on a horizontal part. The time variable t is omitted from the equations. (b) Similarly for recording v_z following Equation (9). (c) Similarly for recording τ_{xz} following Equation (10).

$$\tilde{\delta}_{hxz}(\mathbf{x} - \mathbf{x}_{emt}) = \begin{cases} 0 & \text{for } \mathbf{n}(\mathbf{x}_{emt}) = \mathbf{n}^V \\ \sum_{l=1}^L \alpha_l [\delta(\mathbf{x} - \mathbf{x}_{-l}) + \delta(\mathbf{x} - \mathbf{x}_l)] & \text{for } \mathbf{n}(\mathbf{x}_{emt}) = \mathbf{n}^H \\ \text{where } \mathbf{x}_{-l} = (i+1/2, j+1/2-l) \text{ and } \mathbf{x}_l = (i+1/2, j-1/2+l) & \end{cases} \quad (13)$$

and

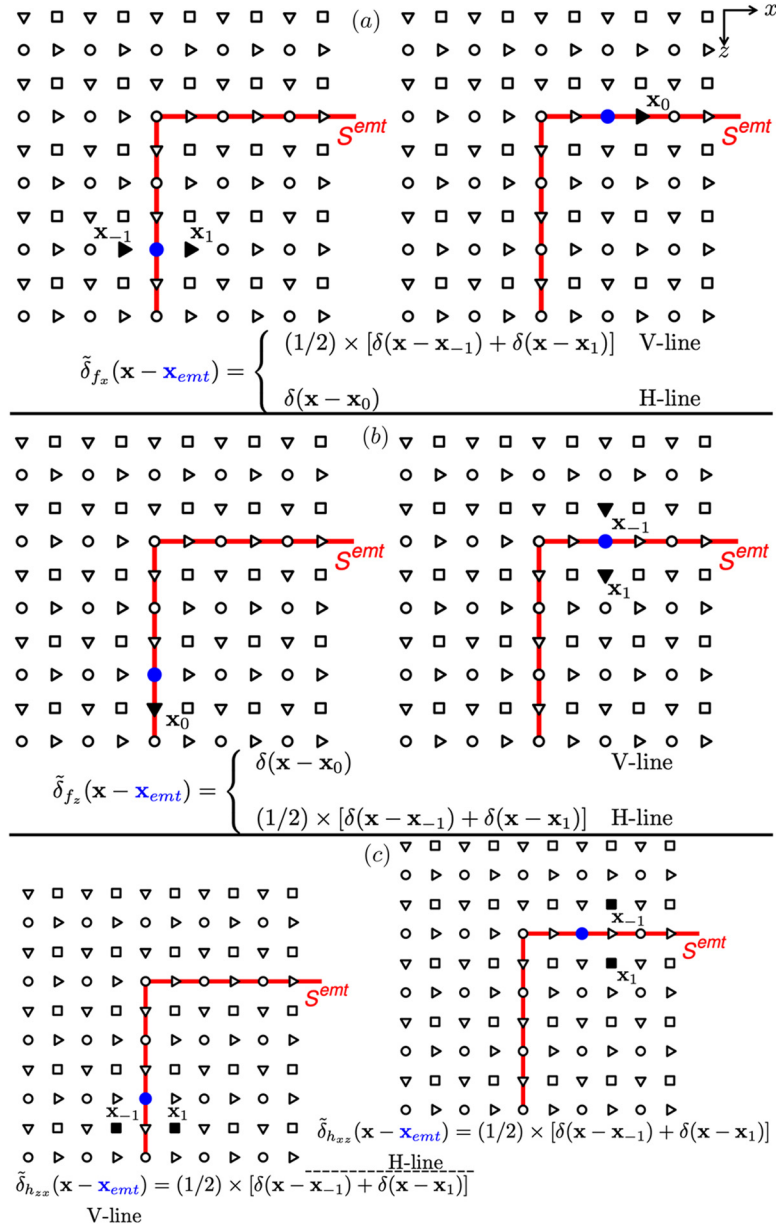


Fig. 4. (Colour online) MPS wavefield injection in the $O(2,2)$ FD scheme. Each panel contains two plots for implementing a source (blue dot) located on a vertical part (left plot) and a horizontal part (right plot) of S^{emt} ; the solid black symbols denote the corresponding *actual* wavefield injection on one or multiple FD nodes. The equations in each panel are associated with the two plots. (a) The source injection scheme for f_x . The equations are the same as in Equation (11) with $L = 1$, ‘V-line’ denotes the case where the source is located on a vertical part of S^{emt} and ‘H-line’ denotes the case where the source is located on a horizontal part. (b) The source injection scheme for f_z , following Equation (12). (c) The source injection schemes for h_{xz} and h_{zx} , following Equations (13) and (14), respectively.

$$\tilde{\delta}_{h_{zx}}(\mathbf{x} - \mathbf{x}_{emt}) = \begin{cases} \sum_{l=1}^L \alpha_l [\delta(\mathbf{x} - \mathbf{x}_{-l}) + \delta(\mathbf{x} - \mathbf{x}_l)] \\ \text{where } \mathbf{x}_{-l} = (i + 1/2 - l, j + 1/2) \text{ and } \mathbf{x}_l = (i - 1/2 + l, j + 1/2) & \text{for } \mathbf{n}(\mathbf{x}_{emt}) = \mathbf{n}^V \\ 0 & \text{for } \mathbf{n}(\mathbf{x}_{emt}) = \mathbf{n}^H \end{cases} \quad (14)$$

Note that the *actual* implementations of h_{xz} and h_{zx} both involve source injection on the FD node τ_{xz} [consider c_{ijkl} in Equation (2)]. Fig. 4 shows examples of implementing individual sources using MPS wavefield injection for the $O(2,2)$ FD scheme with second-order accuracy in both time and space. Another example of MPS in $O(2,4)$ FD modelling (with fourth-order accuracy in space) is presented in Appendix C.

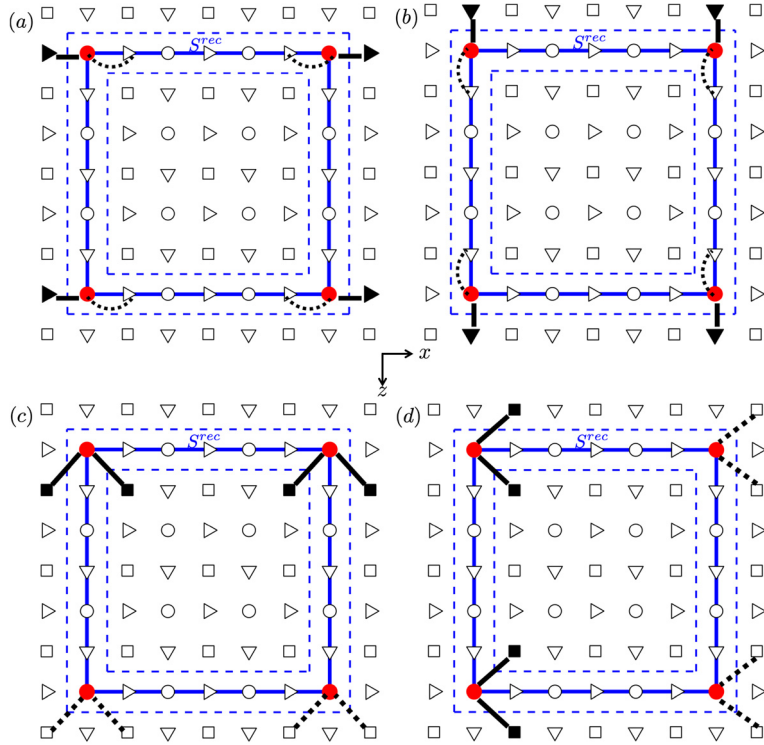


Fig. 5. (Colour online) MPS wavefield recording in the $O(2,2)$ FD scheme at corners. The two dashed blue squares denote the two FD-injection surfaces associated with the MPS recording surface S^{rec} (solid blue square). The red dots denote (only) the locations of measurement points at the four corners. The solid black symbols and thick solid black lines denote relevant, stored wavefield quantities for calculating recordings at corners, while the thick dashed black lines point to wavefield quantities that are excluded in actual recording at corners but would have been used in recording if the measurement point (red dot) is located on the planar surface with which the measurement point is associated. (a) Recording of v_x at the corners for the measurement points on vertical parts of S^{rec} [compared to Fig. 3(a, left) in which a measurement point is on a planar vertical segment of S^{rec} but not at a corner position]. (b) Recording of v_z for the measurement points on horizontal parts of S^{rec} [compared to Fig. 3(b, right)]. (c) Recording of τ_{xz} for the measurement points on vertical parts of S^{rec} [compared to Fig. 3(c, left)]. (d) Recording of τ_{xz} for the measurement points on horizontal parts of S^{rec} [compared to Fig. 3(c, right)]. Otherwise, key as in Fig. 3.

2.3.3. MPS at corners

A subtle but critical point in MPS is the wavefield recording and injection at (sharp) corners of closed (rectangular) surfaces (i.e., S^{rec} and S^{emt}). MPS is limited by the fact that normal directions (i.e., \mathbf{m} for S^{rec} and \mathbf{n} for S^{emt}) at corners cannot be defined. A conventional approach for (2D) MPS at corners is to use a simple weighting factor $1/2$ for each of the vertical and horizontal parts of an MPS surface (i.e., S^{rec} or S^{emt}) that converge at the corners, for both wavefield recording on S^{rec} and source injection on S^{emt} [1,9]. Despite the fact that this approach is successful in acoustic IBCs and provides machine-precision accuracy [64], when applied to elastic IBCs, it results in errors at corners in locally-recomputed wavefields, which subsequently leak into the rest of the local domain.

Here, we propose another solution that relies on linking MPS to FD injection: a wavefield recording and injection method with guaranteed machine-precision accuracy (but at a high computational cost, discussed in Section 2.3.5). In $O(2,2)$ FD modelling, our MPS method (the examples shown in Figs. 3 and 4) with a user-defined MPS surface (i.e., S^{rec} or S^{emt}) coinciding with FD grids can be considered as a superposition of two neighbouring FD-injection surfaces that lie in-between FD grid quantities [58]. Hence, we can follow the wavefield recording and injection schemes at corners in Thomsen et al. [58] to complement our MPS method in $O(2,2)$ FD modelling. The details of linking MPS to FD injection is beyond the scope of this paper and can be found in Thomsen et al. [57]. Here, we focus only on MPS wavefield recording and injection at corners.

Fig. 5 shows MPS wavefield recording in $O(2,2)$ FD modelling at the four corners of a recording surface S^{rec} . Note that each corner of the closed rectangular recording surface S^{rec} is sampled twice, by one measurement point on a vertical segment of S^{rec} and another that is on a horizontal segment. In other words, the two measurement points at the same corner locations are associated with the two line segments of S^{rec} that converge at this corner, respectively. The two FD-injection surfaces shown in Fig. 5 act as auxiliary surfaces to determine wavefield recording at a corner compared to the recording on the same planar surface on which the measurement point (at the corner) is located or with which the point is associated. The principles of wavefield recording at corners are:

- For MPS recordings that are calculated from a wavefield quantity at a single node [e.g., the single solid black symbols in Figs. 3(a, right), (b, left)], the recording at a corner is the same as the recording on the planar surface on which the measurement point is located.
- Otherwise at a corner, two associated quantities [e.g., the two solid black symbols in Fig. 3(a, left)] are stored [for further use in calculations such as those in Equation (8)] during an FD simulation (at each time step) as if the measurement point is located on the planar surface with which it is associated (but not located at a corner position). Wavefield recording at corners depends on (1) whether the stored quantity that is located outside S^{rec} is also located outside the outer FD-injection surface and (2) whether the other stored quantity that is located inside S^{rec} is also located inside the inner FD-injection surface. If (1) and (2) are both true [e.g., Fig. 5(c), upper left and right corners], both stored quantities are kept in order to calculate the final recording using the same MPS scheme presented in Section 2.3.1. If (1) is true but (2) is false [e.g., Fig. 5(a)], only the stored quantity in (1) is kept (or scaled by one) while the quantity in (2) is set to zero (or scaled by zero) in the MPS recording scheme. The case that (2) is true and (1) is false does not exist in the geometry shown in Fig. 5.
- When both stored quantities are outside of the outer FD-injection surface [e.g., Fig. 5(c), lower left and right corners], the two quantities are both set to zero.

Note that in Fig. 5, the thick solid and dashed lines are used only to show the relevant and irrelevant wavefield quantities associated with wavefield recordings at corners, following the principles listed above. Normal stresses τ_{xx} and τ_{zz} can be obtained directly at the locations of the measurement points at corners, and hence Fig. 5 does not include this straightforward recording.

Following the same principles as for MPS wavefield recording, the system used for MPS injection at corners of S^{emt} is depicted in Fig. 6. Similar to MPS recording, two co-located sources are assigned for each corner formed by the convergence of a horizontal and a vertical line segment of S^{emt} . Note that for h_{zx} sources in the geometry shown [Fig. 6(c)], wavefield injection at the lower two corners does *not* happen (or equivalently, a zero value is injected onto FD grids). A similar situation occurs in the implementations of h_{xz} sources at the right two corners [Fig. 6(d)]. The principles of using two FD-injection surfaces to determine wavefield recording and injection at corners can be extended to higher-order FD modelling, as presented in Appendix C.

2.3.4. Pre-computing the Green's functions for the Kirchhoff-Helmholtz extrapolation integrals

The Green's functions needed in the Kirchhoff-Helmholtz extrapolation integrals [i.e., Equations (6) and (7)] are computed using time-domain FD simulations on a full model, using the same FD scheme that is used in the IBC simulation over the local domain. In these FD simulations on the full model, sources are placed at locations on the recording surface S^{rec} while the recordings are made at locations on the emitting surface S^{emt} . Note that in theory Green's functions involve impulsive point sources, i.e., a δ distribution in both time and space. In FD modelling with time- and space-discretised representations of wavefield quantities, wavefield injection for point sources on S^{rec} is implemented using the MPS method. For an impulsive source, wavefield injection *only* occurs at time $t = 0$ or the first time step (Δt) with the injected value $1/(\Delta x \Delta z \Delta t)$. Wavefield recording (i.e., impulse responses) on S^{emt} is also implemented with MPS. Evaluations of the Kirchhoff-Helmholtz integrals for the wavefield extrapolation in IBCs are carried out in the time-discrete forms presented in Appendix B.

2.3.5. IBCs implemented with FD injection

If computational resources allow, local wavefield modelling based on IBCs can also be implemented directly using FD injection with guaranteed machine-precision accuracy [30,34]. This implementation is entirely different from treating MPS as two FD injections, as presented in Section 2.3.3 and is, in general, applicable to higher-order FD modelling and any other wave equations. However, using FD injection to implement IBCs costs significantly more computational and memory storage resources than using MPS. The general (acoustic) algorithm of using FD injection for immersive wavefield modelling can be found in van Manen et al. [30], and in this paper, we extend the algorithm to elastic wave equations and implement elastic IBCs.

FD injection is a general two-step wavefield recording and injection method for any wave equation that is linear for the principle of superposition and for any spatial gradient operator (e.g., FD stencils) that is compact in space. For the elastic wave equations shown as Equations (1) and (2) and the 2D velocity-stress FD scheme introduced by Virieux [65], wavefield recording and injection based on FD injection are summarised in the following. We refer to Robertsson and Chapman [47] for more details.

- During an initial FD simulation, we focus on update wavefield quantities whose FD stencils cross a user-defined boundary, i.e., an FD-injection surface (e.g., inner or outer dashed blue square in Fig. 5) that lies in-between FD gridpoints. For an update quantity that is located inside of the FD-injection surface, the wavefield quantity(s) on the part of the stencil outside the FD-injection surface should be recorded. For an update quantity that is located outside of the FD injection surface, stencil quantity(s) inside the FD-injection surface should be recorded.
- Subsequently in a second simulation, wavefield injections are carried out at the locations of the updated wavefield quantities whose FD stencils cross an FD-injection surface (i.e., for those gridpoints for which quantities were recorded in the first step). For an update quantity that is located inside of the FD-injection surface, the injected value is calculated

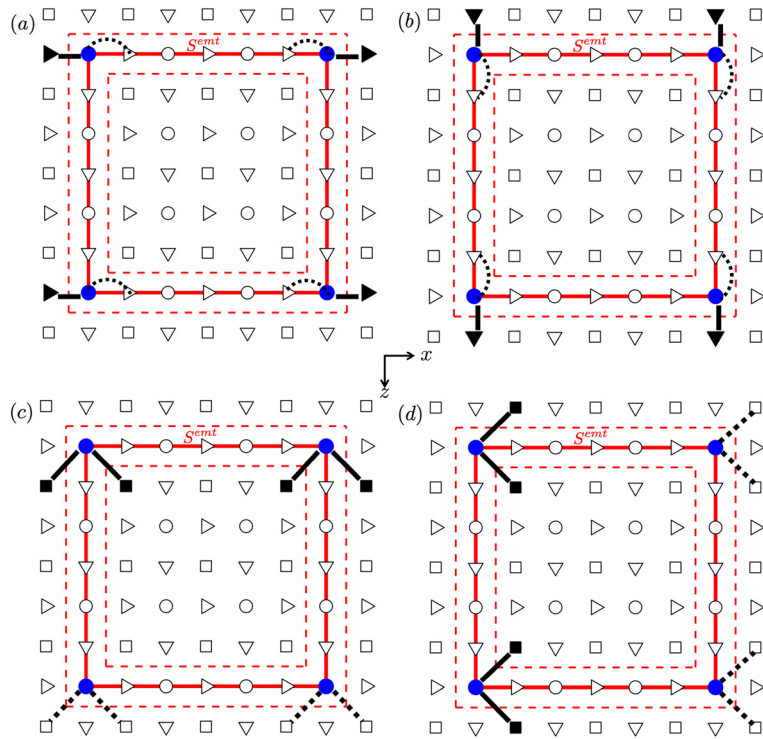


Fig. 6. (Colour online) MPS wavefield injection in the O(2,2) FD scheme at corners. The two dashed red squares denote the two FD-injection surfaces associated with the MPS injection surface S^{emt} (solid red square). The blue dots denote the sources placed at the four corners of S^{emt} . The solid black symbols and thick solid black lines denote actual wavefield injection for sources (blue dots) at corners, while the thick dashed black lines point to wavefield injection that does not actually happen but should be carried out if the source is located on the planar surface with which the source is associated. (a) f_x source injection at the corners that are associated with the vertical parts of S^{emt} [compared to Fig. 4(a, left) in which a source is on a planar vertical segment of S^{emt} but not at a corner position]. (b) f_z source injection at the corners on horizontal parts of S^{emt} [compared to Fig. 4(b, right)]. (c) h_{xz} source injection at the corners on vertical parts of S^{emt} [compared to Fig. 4(c, left)]. (d) h_{xz} source injection at the corners on horizontal parts of S^{emt} [compared to Fig. 4(c, right)]. Otherwise, key as in Fig. 4.

from the recorded wavefields at the FD gridpoints that are on the FD stencil (for the update quantity) outside the FD-injection surface. The calculation follows the FD update such that the FD stencil is corrected for the wavefield inside of the injection surface to appear from outside. For an update quantity that is outside of the FD-injection surface, the injected value is calculated from wavefields at the FD gridpoints inside the FD-injection surface.

Wavefield extrapolation can also be implemented using FD injection, as illustrated in van Manen et al. [30]. In an IBC simulation implemented with FD injection, both the emitting surface S^{emt} and the recording surface S^{rec} lie in-between FD grid quantities; this differs from the setup of S^{emt} and S^{rec} in the method of MPS where they coincide exactly with grid lines, as shown in Fig. 2(b). For wavefield extrapolation, wavefield recordings are made at each FD gridpoint whose FD stencil crosses S^{rec} (i.e., an FD-injection surface). The recording for each gridpoint is calculated from the wavefield quantities that are on the stencil but on the opposite side of S^{rec} , and the calculation follows the same wavefield injection scheme as in FD injection introduced above. Also, one needs to (pre-)compute FD Green's functions that connect each FD-injection-related gridpoint around S^{rec} and each gridpoint around S^{emt} [for the definition of FD Green's functions, see Ref. 30]. The wavefield injection around S^{emt} is carried out using FD injection with injected values calculated from extrapolated wavefield quantities. Note that compared to MPS, wavefield recording and injection in FD injection do not depend on a surface normal vector; instead, they depend on locations of sources/receivers inside or outside of an FD injection surface.

In IBCs implemented by FD injection, the sources on S^{emt} and receivers or measurement points on S^{rec} are distributed across multiple layers, depending on the length of FD stencil used in numerical simulations; this is different from the single-layer sources and measurement points used in the IBC simulations implemented with MPS. Hence, implementing IBCs with FD injection takes more computational power and memory than those implemented with MPS, due to more sources and measurement points (receivers) used and more pre-computed Green's functions that connect these sources and measurement points in the FD-injection-based IBCs [see Ref. 30, and more discussion in Section 4]. Hence, for applications that do not necessarily require machine-precision accuracy or in the simulations of IBC-based physical experiments where the number of physical sources and receivers must be kept to a minimum [6,8,66], MPS may be preferable over FD injection due to considerations of cost.

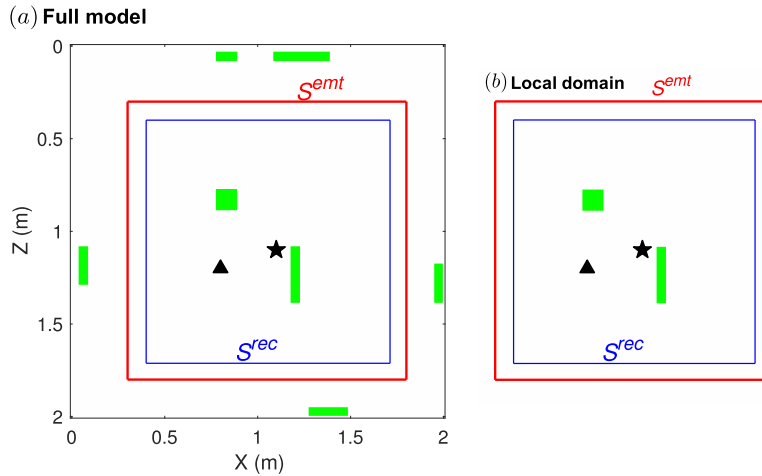


Fig. 7. (Colour online) (a) Two-dimensional full model for IBCs with background density ρ_0 (white region), and with scatterers of density $6\rho_0$ (green). The blue and red squares represent the recording surface S^{rec} and emitting surface S^{emt} , respectively. The black star shows a local source that generates wave energy for both the reference simulation on the full model and the IBC simulation in the sub-domain (inside S^{emt}). The black triangle denotes a local receiver. (b) Local domain (inside S^{emt}) where an IBC simulation is carried out.

Table 1
Numerical values of the model parameters used.

Parameter	Definition	Value
c_p	compressional wave velocity	5450 m/s
c_s	shear wave velocity	3200 m/s
ρ_0	background density	2000 kg/m ³
l_x	length of model	2 m
l_z	width of model	2 m
f_p	peak frequency of Ricker wavelet	10 kHz
t_{max}	time length of simulation	1.5 ms
Δt	time step	8.8073×10^{-7} s
Δx	finite-difference grid size in x direction	$0.016 \text{ m} (\frac{1}{20} c_s / f_p)$
Δz	finite-difference grid size in z direction	$0.016 \text{ m} (\frac{1}{20} c_s / f_p)$

3. Numerical examples

Fig. 7 shows a 2D model for IBCs with homogeneous compressional and shear velocities c_p and c_s and heterogeneities of density $6\rho_0$ where ρ_0 is the background density across the rest of the domain. In Table 1, we summarise the model and FD simulation parameters. IBC simulations are performed only in the local domain [Fig. 7(b)], truncated by the emitting surface S^{emt} from the full model [Fig. 7(a)]. An explosive deformation rate source is placed inside the local domain, and the source signature corresponds to a Ricker wavelet with peak frequency $f_p = 10$ kHz [69]. For the reference simulation performed on the full model, perfectly matched layers (PMLs) [48] are implemented to absorb the wavefield propagating outside of the model.

The Green's functions used for wavefield extrapolation [i.e., Equations (6) and (7)] in IBCs are computed using time-domain FD simulations on the full model shown in Fig. 7, except that the domain inside the recording surface S^{rec} was taken to be homogeneous. For IBC simulations carried out after computing these Green's functions, the scatterers inside the recording surface S^{rec} in Fig. 7 can therefore be treated as medium perturbations (from a homogeneous local model), which are *not* included in the pre-computed Green's functions used for wavefield extrapolation. In theory, IBCs allow the scatterers inside S^{rec} to be changed arbitrarily for local wavefield (re)computation such that all higher-order long-range interactions between local and global domains are correctly computed.

IBC can be implemented with an accuracy of machine precision (compared to global-domain simulations) using FD injection since wavefield recording and injection based on FD injection relies on the linearity of FD operators and hence naturally is as accurate as machine precision allows [30,34]. The second column of Fig. 8 shows the IBC simulation implemented using FD injection on the model shown in Fig. 7, together with the reference simulation (first column) on the full model shown in Fig. 7. Here, we use the FD modelling scheme with second-order accuracy in both time and space [i.e., $O(2,2)$]. In the third column of Fig. 8, we show that the locally-computed wavefield is exact to machine-precision accuracy with the error at a relative order of magnitude of 10^{-12} . However as we have mentioned above and will discuss further in Section 4, the computational cost of using FD injection for IBCs may become a major bottleneck since the number of sources and measurement points (receivers) involved on emitting and recording surfaces increases with the spatial order of

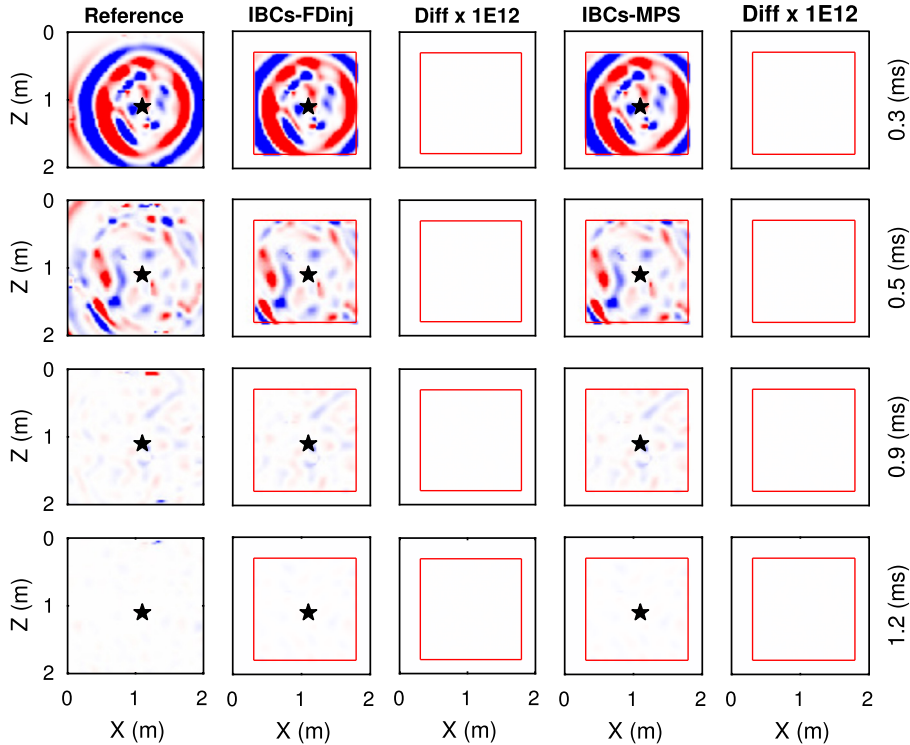


Fig. 8. (Colour online) Snapshots of the IBC simulations implemented with FD injection and MPS in $O(2,2)$ FD modelling. The first column shows the reference FD wavefield τ_{xx} at different times, and the black star represents the local source shown in Fig. 7. The second column shows the IBC simulation implemented with FD injection, and the fourth column shows the IBC simulation implemented with MPS. The third and fifth columns show the difference in the local domain between the IBC (second and fourth columns) and reference (first column) simulations, exaggerated by a factor of 10^{12} (1E12).

FD modelling. Due to this limitation, we do not implement numerical examples of IBCs using FD injection for higher-order FD modelling.

The fourth column of Fig. 8 shows the IBC simulation implemented using the MPS method on the model shown in Fig. 7. Here we still implement IBCs in $O(2,2)$ FD modelling. The local wavefield simulated in the sub-domain exactly matches the reference wavefield simulated on the global model, and the error is as low as machine calculations allow (see the fifth column of Fig. 8). Hence in $O(2,2)$ FD modelling, both MPS and FD injection can be used to implement elastic IBCs to machine-precision.

Fig. 9 shows the $O(2,4)$ IBC simulation (with fourth-order FD accuracy in space) implemented using MPS on the model shown in Fig. 7. In this IBC simulation, the sub-domain enclosed by the emitting surface S^{emt} is simulated with extra PMLs deployed outside of S^{emt} such that any outward-propagating wavefield that is not perfectly cancelled at S^{emt} (e.g., at corners) can be further attenuated outside S^{emt} . In Fig. 9, we show some error that originates around the corners of the emitting surface S^{emt} (second row of Fig. 9) and propagates into the whole sub-domain. This corner-related error is small, and the difference between the IBC and reference wavefields is exaggerated by a factor of 1000 to be visible. In Fig. 10, we further compare the recorded signals at the local receiver (i.e., the black triangle in Fig. 9) in both wavefields and show that the error of recomputing wavefields in a local domain is negligible in this higher-order FD modelling scheme [i.e., $O(2,4)$]. We also found that using the new paradigm of wavefield recording and injection at corners improves the accuracy of higher-order FD-based IBC implementations by one order of magnitude compared to using the conventional approach, i.e., the factor $1/2$ described in Section 2.3.3 (this less accurate IBC simulation is not shown).

Our observation from the IBC simulation suggests that the corners may be responsible for all of the inaccuracy. To further explore the (potential) origin(s) of the observed error, we use a fully homogeneous IBC model shown in Fig. 11. The values of the model parameters in Table 1 are used except for $l_x = 6$ m. In this case, the immersive boundary condition (IBC) applied on the emitting surface S^{emt} becomes an absorbing boundary condition [15,18,61], and all outgoing waves (i.e., ray path 1 in Fig. 1), ideally, should be perfectly cancelled at S^{emt} .

Fig. 12 shows the IBC simulation corresponding to the model shown in Fig. 11, with the $O(2,4)$ FD scheme. The error of (re)-computing wavefields locally in this MPS-based IBC simulation is mainly caused by the corners, while some artefacts exist along the two horizontal line segments of the emitting surface S^{emt} . These artefacts move horizontally and are referred to as 'halo' artefacts in Vasmel and Robertsson [63], which are caused by the long FD stencil updating (with $2L \geq 4$) across the emitting surface S^{emt} together with the MPS wavefield injection on S^{emt} . These halo artefacts do not exist in the IBC simulations implemented with FD injection.

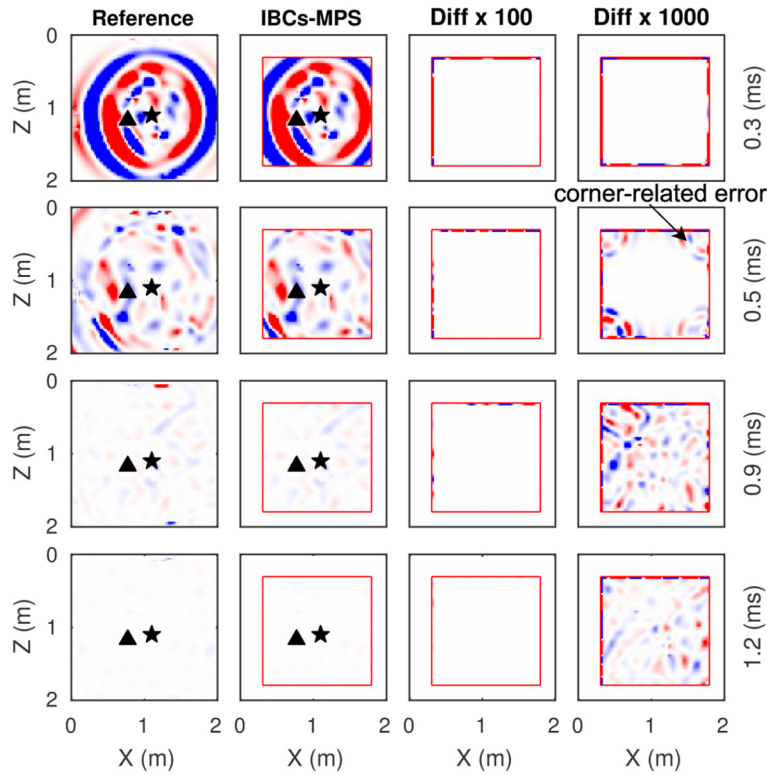


Fig. 9. (Colour online) Snapshots of the IBC simulation implemented with MPS in $O(2,4)$ FD modelling. Key for the first and second columns as in Fig. 8, and the black triangle denotes the local receiver shown in Fig. 7. The third and fourth columns show the difference between the reference and IBC simulations exaggerated by a factor of 100 and 1000, respectively.

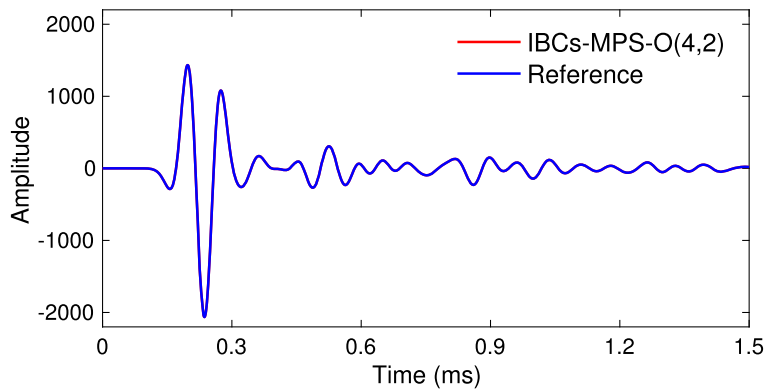


Fig. 10. (Colour online) Recorded traces at the local receiver (i.e., the black triangle in Fig. 9) in the reference $O(2,4)$ FD simulation and IBC simulation implemented with MPS.

4. Discussion

Linking an MPS method to FD injection helps to eliminate the limitation in conventional MPS at corners where a surface normal vector cannot be defined. This is due to the fact that FD injection does not involve the concept of a surface normal at all for wavefield recording and injection [47]. However in higher-order FD modelling, this strategy of linking MPS to FD injection does not generalise in a straightforward manner. In this paper, we simply extend $O(2,2)$ MPS at corners to a higher-order scheme [i.e., $O(2,4)$] without expecting machine-precision accuracy in the implementations of IBCs. This new scheme used specifically at corners improves accuracy over the scheme that simply uses the factor of $1/2$ to weight contributions on each of the converging surface edges as was proposed by Vasmel and Robertsson [63] for acoustic MPS. Whether a better MPS scheme might be possible for machine-precision accuracy in higher-order FD modelling remains an open issue.

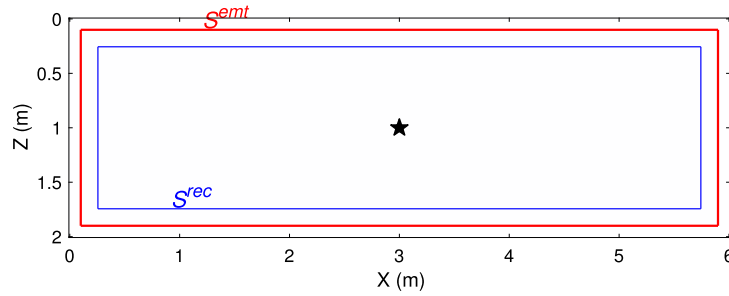


Fig. 11. (Colour online) Homogeneous IBC model. Key as in Fig. 7.

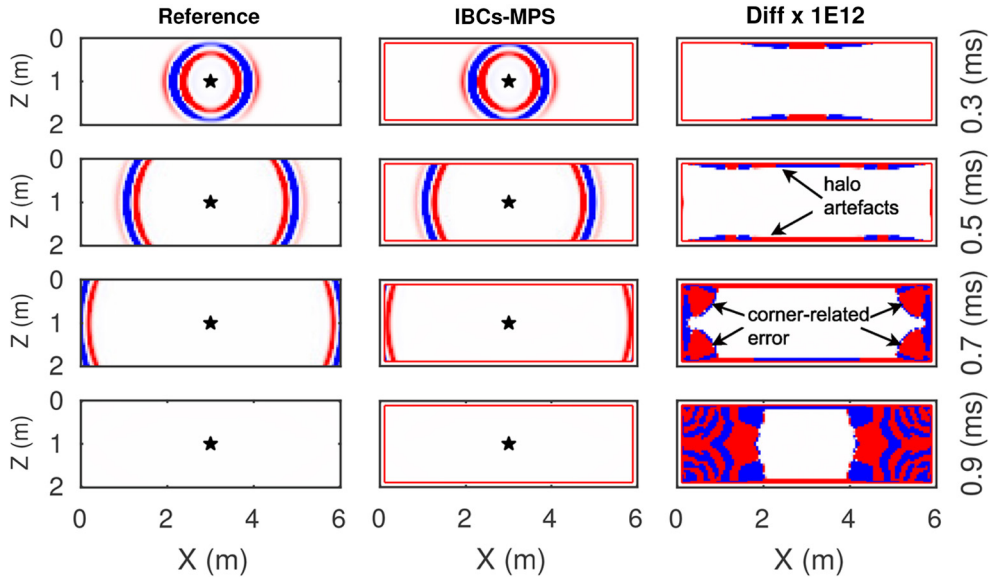


Fig. 12. (Colour online) Snapshots of the $O(2,4)$ IBC simulation implemented with MPS on the model shown in Fig. 11. Key as in Fig. 8.

When using IBCs for local-domain modelling, the computationally single most expensive operation is the wavefield extrapolation, in which the pre-computed Green's functions also occupy a large amount of memory. IBCs are non-local in both time and space, requiring significant overhead of computational and memory storage resources [9,30]. The computational cost of the wavefield extrapolation is estimated with $O(n_{emt} \times n_{rec} \times N_t^3)$ where n_{emt} represents the number of sources at an emitting surface S^{emt} , n_{rec} represents the number of measurement points (receivers) at a recording surface S^{rec} , and N_t represents total time steps of numerical simulations. The memory storage cost is estimated with $O(n_{emt} \times n_{rec} \times N_t)$. These cost estimates apply to both IBCs implemented with MPS and FD injection, but IBCs with FD injection is even more expensive than IBCs with MPS, especially in higher-order FD modelling. This is because in IBCs with FD injection, the number of sources on S^{emt} and measurement points (receivers) on S^{rec} linearly increases with the length of FD stencil or the spatial order of FD modelling, i.e., $n_{emt} \propto L$ and $n_{rec} \propto L$; in contrast, in IBCs with MPS, the number of sources and receivers does not change with the length of FD stencil. Hence, the computational saving of using MPS over FD injection in IBCs would be $O(L^2)$. For example, the modelling runs of Robertsson et al. [45] (in which FD injection is deployed to perform wavefield separation) used a fourth-order accurate FD scheme. In this scenario for IBCs, we estimate that the saving would amount to a factor ~ 16 in terms of memory and calculations, which is extremely significant for simulations which may already approach the limits of available computational power. The savings would be far larger for higher-order FD schemes, such as in the modelling runs of Vasmel and Robertsson [63] (MPS for local wavefield reconstruction) where a twelfth-order FD scheme is used (so the saving is of a factor ~ 144).

Our IBCs, in practice, require the separation of a recording surface S^{rec} and an emitting surface S^{emt} in space (see Fig. 1). In FD modelling, the number of gridpoint(s) between S^{rec} and S^{emt} should be larger than or equal to the length of the FD stencil ($2L$) [see also Ref. 30]. An intriguing question therefore still remains: can S^{rec} and S^{emt} be collocated in IBCs? We note that IBCs are closely related to the exact non-reflecting boundary conditions, in which S^{emt} encloses all scatterers in the entire model and source injection on S^{emt} cancels all outgoing waves, providing absorbing boundary conditions for numerical simulations [e.g., 15–17,50,61]. Among those works, Teng [56] explored a case where a recording surface coincides with an emitting surface; this involves solving a boundary integral equation (BIE) in conjunction with the wave equation.

Although collocating recording and emitting surfaces has been done by Teng [56] for absorbing boundary problems (i.e., homogeneous global model), Schuster [51] proposes a self-interaction operator which is built from a set of BIEs for a single volume scatterer placed in a global domain. For IBCs, one possible research route is to build a similar set of BIEs when collocating the recording and emitting surface; this results in a system that can be solved using a pure BIE method [29]. Collocating recording and emitting surfaces in IBCs will require a practical numerical means of avoiding the singularities in pre-computed Green's functions that occur from any point to itself in wavefield extrapolation. One potential solution is to consider the approach in Halliday and Curtis [20] and Vasconcelos et al. [62] where source and receiver arrays are collocated, in which one makes use of the fact that these singularities are only relevant for the direct wave between a point and itself, which need not be extrapolated in IBCs. The further development of IBCs with collocated recording and emitting surfaces could also be useful for the development of elastic immersive experimentation in a physical laboratory [e.g., see Ref. 59]. We leave this development for future research.

5. Conclusion

We introduced immersive boundary condition (IBC) theory for elastic local wavefield (re)computation that includes all higher-order long-range interactions between the simulated local domain and global domain. Using IBCs allows local-domain modelling with arbitrary medium perturbations inside the recording surface (of the local domain), and this important feature is provided by the active boundary condition around the local domain, which is updated by means of calculating the Kirchhoff-Helmholtz extrapolation integrals at each time step of an IBC simulation.

We proposed a new method of multiple point sources (MPS) for implementing elastic IBCs in a 2D velocity-stress finite-difference (FD) framework. The MPS method used in an $O(2,2)$ FD scheme (with second-order accuracy in both time and space) is linked to FD injection such that wavefield recording and injection at sharp corners of closed (rectangular) surfaces can be perfectly exact, instead of using a conventional approach that is simply using the factor $1/2$ to weight contributions on each of the converging surface edges. Such a paradigm at corners can also be extended to a higher-order FD modelling scheme [e.g., $O(2,4)$ herein for second-order accuracy in time and fourth-order accuracy in space].

Examples of IBC simulations implemented in $O(2,2)$ FD modelling show that the proposed MPS scheme produces locally-computed wavefields that are accurate to within machine precision compared to global-domain simulations. In higher-order FD modelling, the MPS scheme is still highly accurate, with a remaining error that is two orders of magnitude smaller than the simulated wavefield. This error when simulating a local wavefield is mainly caused by the corners of closed surfaces used in the MPS recording and injection schemes. In higher-order FD modelling, the use of MPS also leads to halo artefacts that move along the planar surfaces of emitting surfaces. In $O(2,2)$ FD modelling, we also implemented elastic IBCs using FD injection, which naturally outputs numerically exact locally-computed wavefields. However, IBCs with FD injection in higher-order FD modelling is intractable due to a significantly increased cost.

We anticipate that the IBC theory and numerical implementations developed in this paper will have further applications in the fields of exploration geophysics (e.g., simulations of wave-based imaging and monitoring surveys), global seismology (e.g., full waveform inversion), nondestructive testing (e.g., imaging localised damaged zone), and medical acoustics related to imaging and inversion in which local-domain modelling can save significant computational cost.

Declaration of competing interest

The authors declare that they have no known competing financial interests or personal relationships that could have appeared to influence the work reported in this paper.

Acknowledgements

We thank an anonymous reviewer for the positive comments. We would like to thank Henrik Thomsen for the discussion about FD injection. This project has received funding from the European Research Council (ERC) under the European Union's Horizon 2020 research and innovation programme (grant agreement No 694407).

Appendix A. Deriving the elastic representation theorem

We consider elastic wave propagation in two states, A and B, which are described by two sets of wave equations of the form as in Equations (1) and (2), as shown in Fig. A.13. Since an impulsive point source exists in state B, the wavefields $\tau_{ij}^B(\mathbf{x}, t)$ and $v_i^B(\mathbf{x}, t)$ become Green's tensors:

$$\tau_{ij}^B(\mathbf{x}, t) \triangleq G_{ij,n}^{\tau,f}(\mathbf{x}, t | \mathbf{x}_b, 0) \quad (\text{A.1})$$

and

$$v_i^B(\mathbf{x}, t) \triangleq G_{i,n}^{v,f}(\mathbf{x}, t | \mathbf{x}_b, 0) \quad (\text{A.2})$$

as the impulse responses of the medium associated with state B. We then consider the *interaction quantity*

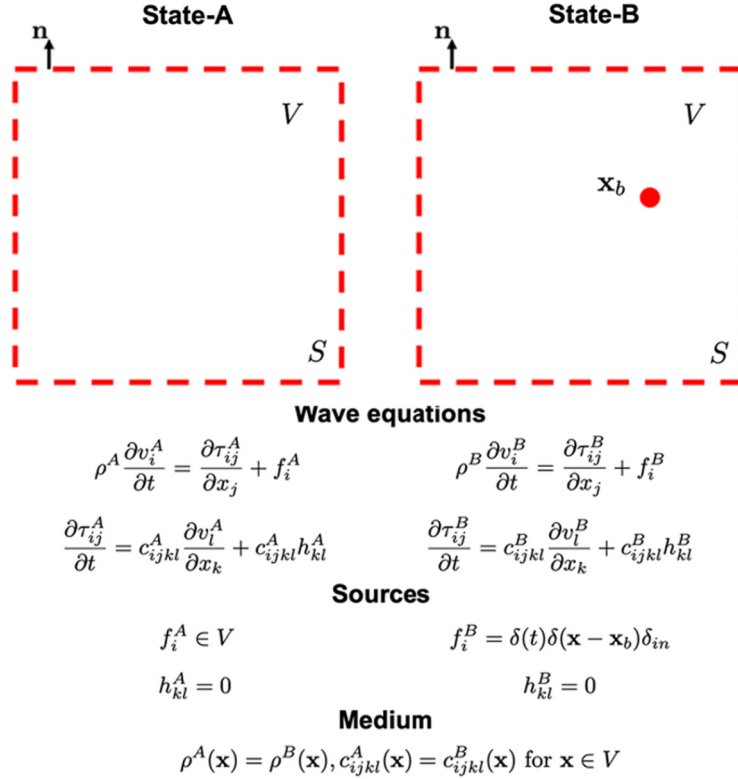


Fig. A.13. (Colour online) Elastic states A and B used to derive the representation theorem. The volume V is enclosed by the surface S with normal vector \mathbf{n} . In state A, body force source(s) exists inside V . In state B, an impulsive body force source in the \mathbf{x}_n direction is placed in V .

$$\partial_j (\tau_{ij}^A * v_i^B - \tau_{ij}^B * v_i^A)$$

where ∂_j is short for the first-order spatial gradient operator $\partial/\partial x_j$. This interaction quantity is integrated over the volume V shown in Fig. A.13, and applied with the divergence theorem of Gauss:

$$\iiint_V \partial_j (\tau_{ij}^A * v_i^B - \tau_{ij}^B * v_i^A) dV = \oint_S (\tau_{ij}^A * v_i^B - \tau_{ij}^B * v_i^A) n_j dS \quad (\text{A.3})$$

to convert the volume integral into a surface integral [4]. The terms inside of the volume integral on the left side of Equation (A.3) are substituted together with the wave equations and source conditions presented in Fig. A.13, and using Equations (A.1) and (A.2) and the definitions of medium properties in states A and B (also presented in Fig. A.13) simplifies Equation (A.3) to

$$v_n^A(\mathbf{x}_b, t) = \int G_{i,n}^{v,f}(\mathbf{x}, t | \mathbf{x}_b, 0) * f_i^A(\mathbf{x}, t) dV(\mathbf{x}) + \oint_S (\tau_{ij}^A(\mathbf{x}, t) * G_{i,n}^{v,f}(\mathbf{x}, t | \mathbf{x}_b, 0) - v_i^A(\mathbf{x}, t) * G_{ij,n}^{\tau,f}(\mathbf{x}, t | \mathbf{x}_b, 0)) n_j dS(\mathbf{x}) \quad (\text{A.4})$$

where n_j is the normal vector component of S enclosing V in Fig. A.13.

We apply elastic source-receiver reciprocity [53,70]:

$$G_{i,n}^{v,f}(\mathbf{x}, t | \mathbf{x}_b, 0) = G_{n,i}^{v,f}(\mathbf{x}_b, t | \mathbf{x}, 0)$$

and

$$G_{ij,n}^{\tau,f}(\mathbf{x}, t | \mathbf{x}_b, 0) = G_{n,ij}^{v,h}(\mathbf{x}_b, t | \mathbf{x}, 0)$$

to Equation (A.4), which then becomes

$$v_n^A(\mathbf{x}_b, t) = \int G_{n,i}^{v,f}(\mathbf{x}_b, t | \mathbf{x}, 0) * f_i^A(\mathbf{x}) dV(\mathbf{x}) + \oint_S (\tau_{ij}^A(\mathbf{x}, t) * G_{n,i}^{v,f}(\mathbf{x}_b, t | \mathbf{x}, 0) - v_i^A(\mathbf{x}, t) * G_{n,ij}^{v,h}(\mathbf{x}_b, t | \mathbf{x}, 0)) n_j dS(\mathbf{x}) \quad (\text{A.5})$$

as the representation theorem of the convolution type. For IBCs, one can consider the volume V in Fig. A.13 as a sub-domain enclosed by an emitting surface S^{emt} , as shown in Fig. 1. The representation theorem can then be recast as:

$$v_n(\mathbf{x}, t) = \int G_{n,i}^{v,f}(\mathbf{x}, t | \mathbf{x}_s, 0) * f_i(\mathbf{x}_s) dV(\mathbf{x}_s) + \oint_{S^{emt}} (\tau_{ij}(\mathbf{x}_{emt}, t) * G_{n,i}^{v,f}(\mathbf{x}, t | \mathbf{x}_{emt}, 0) - v_i(\mathbf{x}_{emt}, t) * G_{n,ij}^{v,h}(\mathbf{x}, t | \mathbf{x}_{emt}, 0)) n_j dS(\mathbf{x}_{emt}) \quad (\text{A.6})$$

where \mathbf{x}_s is the location(s) of the source(s) inside S^{emt} , and the surface integral on the right-hand side provides the effect of the immersive boundary condition, i.e., Equation (3).

Appendix B. Deriving the elastic Kirchhoff-Helmholtz extrapolation integrals

We define an infinite, unbounded domain with a source that occupies a source domain D_{src} enclosed by a surface ∂D_{src} , as shown in Fig. B.14. The exterior of D_{src} is the volume D'_{src} enclosed by a circular surface S_Δ . Here, we apply the A-B-state analysis based on Equations (1) and (2) (similar to the analysis in Appendix A). The interaction quantity $\partial_j(\tau_{ij}^A * v_i^B - \tau_{ij}^B * v_i^A)$ is integrated over the volume D'_{src} to relate the wavefield quantities in states A and B, defined in Table B.2. The divergence theorem of Gauss is applied to convert the volume integral into the surface integral over the two surfaces, i.e., the exterior surface S_Δ and the interior boundary ∂D_{src} . In view of the causality condition [Ref. 13, equation 5.9] for the surface integral over S_Δ , we have

$$\oint_{S_\Delta} (\tau_{ij}^A * v_i^B - \tau_{ij}^B * v_i^A) s_j dS(\mathbf{x}) = \text{Order}(\Delta^{-1}) \text{ as } \Delta \rightarrow +\infty \quad (\text{B.1})$$

where s_j is the normal vector component of S_Δ . Equation (B.1) shows that the surface integral over S_Δ vanishes as long as the domain D'_{src} is infinitely large or for sufficiently large radius Δ , the volume outside S_Δ has constant material properties, and S_Δ satisfies a Sommerfeld radiation condition. Hence, only the surface integral over the interior boundary ∂D_{src} remains in the A-B-state analysis, which gives

$$v_k^A(\mathbf{x}_b, t) = \oint_{\partial D_{src}} (-\tau_{ij}^A(\mathbf{x}, t) * \Gamma_{i,k}^{v,f}(\mathbf{x}, t | \mathbf{x}_b, 0) + v_i^A(\mathbf{x}, t) * \Gamma_{ij,k}^{\tau,f}(\mathbf{x}, t | \mathbf{x}_b, 0)) m_j dS \quad (\text{B.2})$$

where m_j is the outward-pointing normal vector component of ∂D_{src} , and the Green's functions Γ are associated with state B where the medium in the domain D_{src} has not been defined yet. Similar to Fokkema and van den Berg [13], we change the expressions of the Green's functions in Equation (B.2) using source-receiver reciprocity: $\{\Gamma_{i,k}^{v,f}, \Gamma_{ij,k}^{\tau,f}\}(\mathbf{x}, t | \mathbf{x}_b, 0) = \{\Gamma_{k,i}^{v,f}, -\Gamma_{k,ij}^{v,h}\}(\mathbf{x}_b, t | \mathbf{x}, 0)$. Hence, the elastic Kirchhoff-Helmholtz extrapolation integral reads

$$v_k^A(\mathbf{x}_b, t) = \oint_{\partial D_{src}} (-\tau_{ij}^A(\mathbf{x}, t) * \Gamma_{k,i}^{v,f}(\mathbf{x}_b, t | \mathbf{x}, 0) - v_i^A(\mathbf{x}, t) * \Gamma_{k,ij}^{v,h}(\mathbf{x}_b, t | \mathbf{x}, 0)) m_j dS \quad (\text{B.3})$$

The source field in state B, as defined in Table B.2, can be redefined as $f_i^B(\mathbf{x}) = 0$ and $h_{kl}^B(\mathbf{x}) = \delta(t)\delta(\mathbf{x} - \mathbf{x}_b)\delta_{ki}\delta_{ij}$. In this case, the wavefields associated with state B become Green's tensors $\{\Gamma_{k,ij}^{v,h}, \Gamma_{kl,ij}^{\tau,h}\}(\mathbf{x}, t | \mathbf{x}_b, 0)$. We re-carry out the A-B-state analysis and obtain the Kirchhoff-Helmholtz integral extrapolating for a stress wavefield:

$$\tau_{ij}^A(\mathbf{x}_b, t) = \oint_{\partial D_{src}} (-\tau_{kl}^A(\mathbf{x}, t) * \Gamma_{ij,k}^{\tau,f}(\mathbf{x}_b, t | \mathbf{x}, 0) - v_k^A(\mathbf{x}, t) * \Gamma_{ij,kl}^{\tau,h}(\mathbf{x}_b, t | \mathbf{x}, 0)) m_l dS \quad (\text{B.4})$$

The medium property of state B in the volume D_{src} can be arbitrarily different from the counterpart in state A since in theory, domain D_{src} is not required to be defined to derive Equations (B.3) and (B.4). This implies that computation of the Green's functions does not require knowledge of the medium perturbations inside the recording surface in the simulated sub-domain(s) [9,60], and hence in IBCs, sub-domain simulations always include all higher-order long-range interactions when local medium perturbations take place inside of the recording surface. Note that the derived Kirchhoff-Helmholtz integrals work only for outward wavefield extrapolation. In the case where the extrapolated point \mathbf{x}_b is located inside the

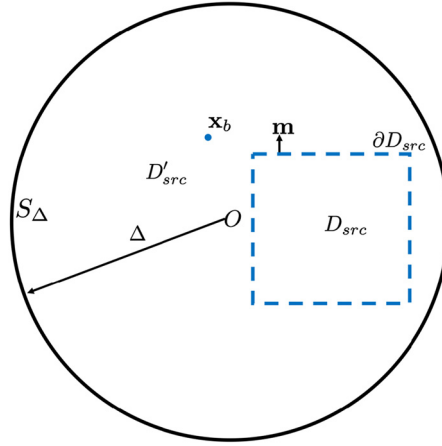


Fig. B.14. (Colour online) Schematic used to derive the Kirchhoff-Helmholtz extrapolation integrals. The vector \mathbf{m} denotes the (outward-pointing) normal to the surface ∂D_{src} . The domain D'_{src} is enclosed by the exterior circular boundary S_Δ with radius Δ , and the point O is the centre of the circle.

Table B.2

Source fields and medium properties of states A and B for deriving the Kirchhoff-Helmholtz extrapolation integrals.

	State A: Actual medium	State B: Green's state
Wavefields	$v_i^A(\mathbf{x}), \tau_{ij}^A(\mathbf{x})$	$v_i^B(\mathbf{x}) = \Gamma_{i,k}^{v,f}(\mathbf{x}, t \mathbf{x}_b, 0), \tau_{ij}^B(\mathbf{x}) = \Gamma_{ij,k}^{\tau,f}(\mathbf{x}, t \mathbf{x}_b, 0)$
Sources	$f_i^A(\mathbf{x}, t) = 0$ $h_{kl}^A(\mathbf{x}, t) = 0$	$f_i^B(\mathbf{x}, t) = \delta(t)\delta(\mathbf{x} - \mathbf{x}_b)\delta_{ik}$ $h_{kl}^B(\mathbf{x}, t) = 0$
Medium	$c_{ijkl}^A(\mathbf{x}) = c_{ijkl}^B(\mathbf{x}), \rho^A(\mathbf{x}) = \rho^B(\mathbf{x})$ for $\mathbf{x} \in D'_{src}$	

source domain D_{src} , the left sides of Equation (B.3) and (B.4) will become zero, which is known as the Oseen's extinction theorem [see Ref. 13].

For IBC simulations, Equations (B.3) and (B.4) are related to Equations (6) and (7) by setting the surface D_{src} as the recording surface S^{rec} in Fig. 1 and the extrapolation point on the emitting surface $\mathbf{x}_b = \mathbf{x}_{emt}$.

In IBC simulations implemented with MPS, the evaluations of Equations (6) and (7) are carried out at each FD time step. Following the same principle used to calculate an acoustic Kirchhoff-Helmholtz extrapolation integral [31], we discretize the temporal convolution in Equations (6) and (7), which give

$$\begin{aligned} \hat{v}_i(\mathbf{x}_{emt}, l, n) = & \hat{v}_i(\mathbf{x}_{emt}, l, n-1) + \\ & \oint_{S_{rec}} \left(-\hat{\tau}_{kl}(\mathbf{x}_{rec}, n) \hat{\Gamma}_{i,k}^{v,f}(\mathbf{x}_{emt}, l-n | \mathbf{x}_{rec}, 0) \right. \\ & \left. - \hat{v}_k(\mathbf{x}_{rec}, n) \hat{\Gamma}_{i,kl}^{v,h}(\mathbf{x}_{emt}, l-n | \mathbf{x}_{rec}, 0) \right) m_l dS(\mathbf{x}_{rec}) \end{aligned} \quad (\text{B.5})$$

and

$$\begin{aligned} \hat{\tau}_{ij}(\mathbf{x}_{emt}, l, n) = & \hat{\tau}_{ij}(\mathbf{x}_{emt}, l, n-1) + \\ & \oint_{S_{rec}} \left(-\hat{\tau}_{kl}(\mathbf{x}_{rec}, n) \hat{\Gamma}_{ij,k}^{\tau,f}(\mathbf{x}_{emt}, l-n | \mathbf{x}_{rec}, 0) \right. \\ & \left. - \hat{v}_k(\mathbf{x}_{rec}, n) \hat{\Gamma}_{ij,kl}^{\tau,h}(\mathbf{x}_{emt}, l-n | \mathbf{x}_{rec}, 0) \right) m_l dS(\mathbf{x}_{rec}) \end{aligned} \quad (\text{B.6})$$

where the hat symbol $\hat{\cdot}$ is used to denote time-discretized quantities. Discrete time indices l and n correspond to t in Equations (6) and (7) and a time step that is iterated from 1 until l (for $l > n$) such that the extrapolated wavefields are recursively calculated. This recursive calculation can be implemented as a matrix-vector multiplication [see Ref. 9].

Appendix C. MPS in higher-order finite-difference modelling

In this appendix, we present the MPS wavefield recording and injection methods in higher-order FD modelling [i.e., $O(2,4)$ for second-order accuracy in time and fourth-order accuracy in space], complementing the $O(2,2)$ scheme presented in Sections 2.3.1, 2.3.2, and 2.3.3.

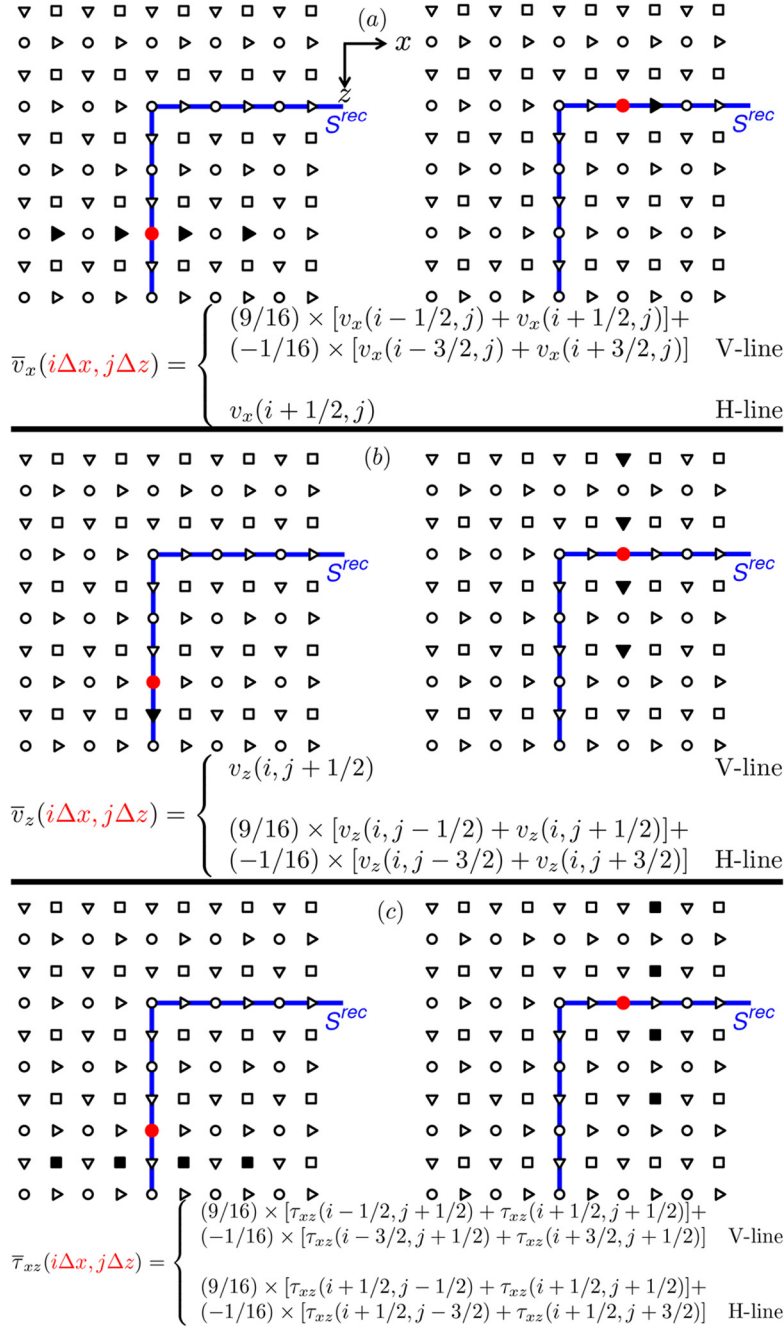


Fig. C.15. (Colour online) MPS wavefield recording in the O(2,4) FD scheme (fourth-order accuracy in space). Key as in Fig. 3.

Fig. C.15 shows MPS wavefield recording along planar surfaces (of S^{rec}) in O(2,4) FD modelling. The interpolation coefficients α_l are $\alpha_1 = 9/16$ and $\alpha_2 = -1/16$. Fig. C.16 shows MPS injection along planar surfaces (of S^{emt}) in O(2,4) FD modelling.

Fig. C.17 shows MPS wavefield recording at corners in O(2,4) FD modelling. We follow similar principles as in the O(2,2) paradigm (Fig. 5). For recording calculated only from a single node of wavefield quantity [i.e., the single solid black symbols in Figs. C.15(a, right), (b, left)], the recording at a corner is the same as the recording on the planar line segment of S^{rec} . Otherwise the wavefield quantities (potentially) involved are first stored as if the measurement point at a corner is located on its associated planar surface, and then these stored wavefield quantities are divided into two sets, depending on whether these quantities are located inside or outside of S^{rec} . One then checks (1) whether the set of stored quantities that are

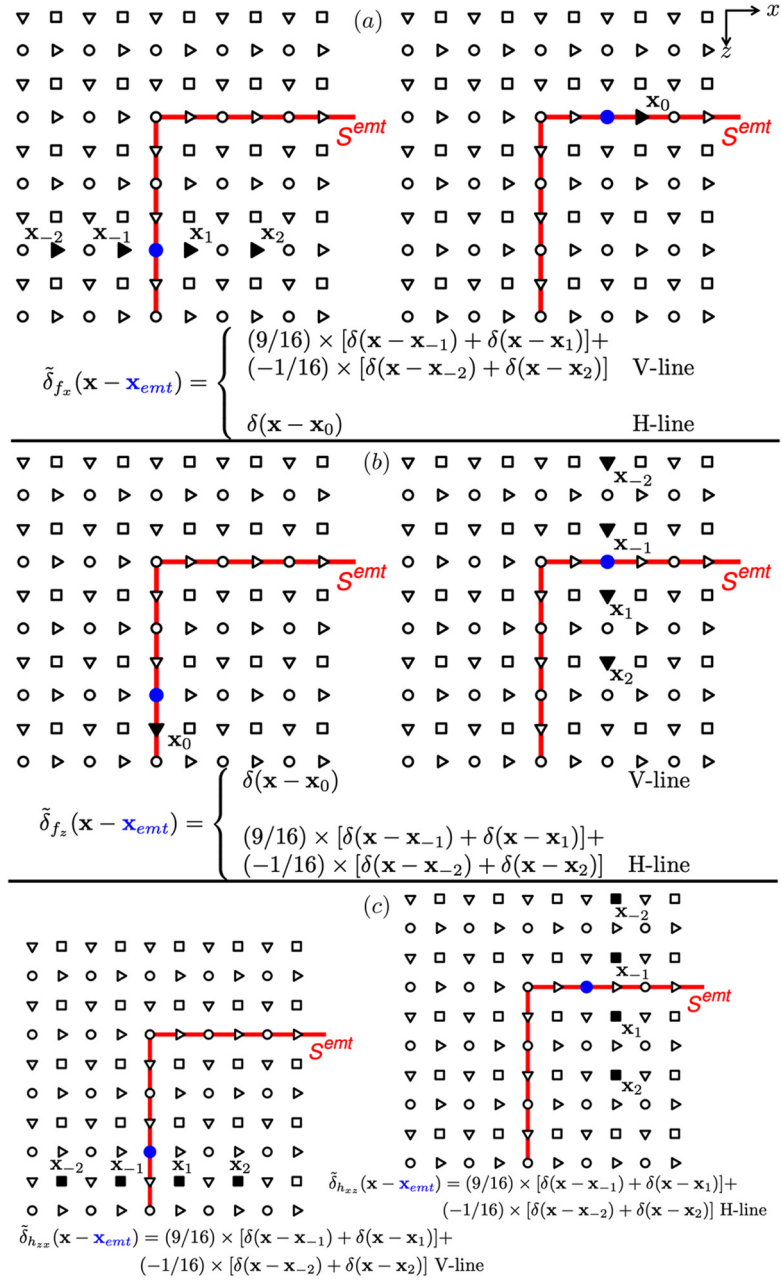


Fig. C.16. (Colour online) MPS wavefield injection in the O(2,4) FD scheme. Key as in Fig. 4.

located outside S^{rec} is also located outside the outer FD-injection surface and (2) whether the other set of stored quantities that are located inside S^{rec} is also located inside the inner FD-injection surface. If (1) and (2) are both true [e.g., Fig. C.17(c), upper left corner], both sets of stored quantities are kept for calculating the recording, following the scheme presented in Section 2.3.1 (with $L = 2$). If (1) is true but (2) is false [e.g., Fig. C.17(a)], only the set of stored quantities in (1) is kept for recording while the quantities in (2) are all set to zero for the wavefield measurement on S^{rec} (i.e., Equations (8), (9), and (10) in Section 2.3.1). When both sets of stored quantities are outside the outer FD-injection surface [e.g., Fig. C.17(c), lower left and right corners], all quantities are set to zero.

Fig. C.18 shows MPS wavefield injection at corners in O(2,4) FD modelling, following the same principles as for MPS wavefield recording. Following the same idea here, our MPS method can be applied to other higher-order (in space) FD modelling schemes.

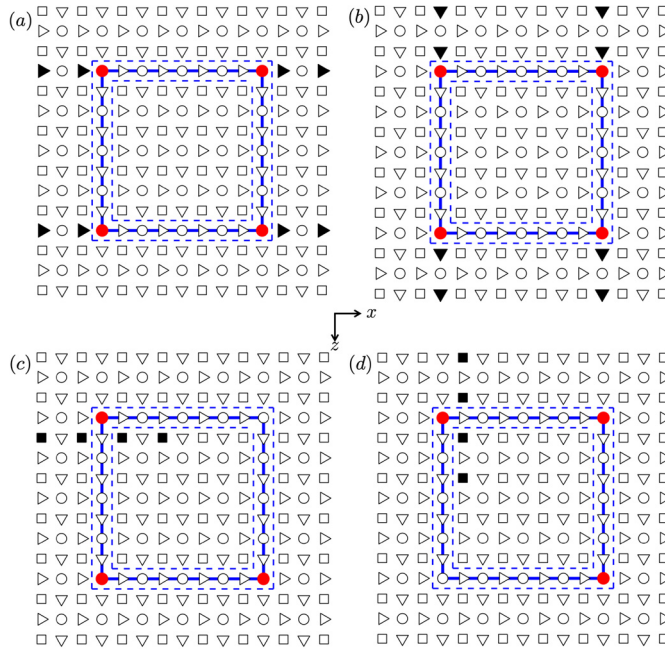


Fig. C.17. (Colour online) MPS wavefield recording in the $O(2,4)$ FD scheme at corners. Key as in Fig. 5. (a) Recording of v_x [compared to Fig. C.15(a, left)]. (b) Recording of v_z [compared to Fig. C.15(b, right)]. (c) Recording of τ_{xz} [compared to Fig. C.15(c, left)]. The recording at the upper right corner is the same as that at the upper left corner but not marked in the graph for visualisation purposes only (i.e., avoiding confusion on the solid black markers associated with the upper left corner). The recordings at the two lower corners are set to zero. (d) Recording of τ_{xz} [compared to Fig. C.15(c, right)]. The recording at the lower left corner is the same as that at the upper left corner (not marked). The recordings at the two right corners are set to zero.

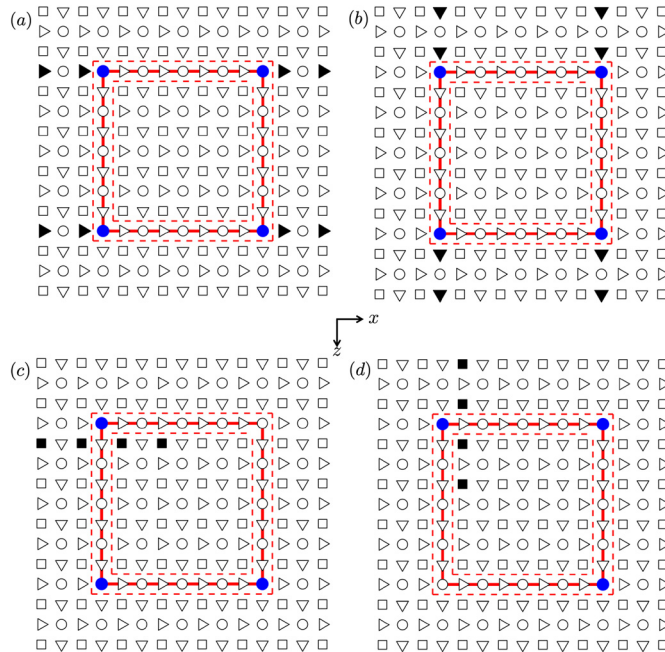


Fig. C.18. (Colour online) MPS wavefield injection in the $O(2,4)$ FD scheme at corners. Key as in Fig. 6. (a) f_x source injection [compared to Fig. C.16(a, left)]. (b) f_z source injection [compared to Fig. C.16(b, right)]. (c) h_{zx} source injection [compared to Fig. C.16(c, left)]. Source injection at the upper right corner is the same as that at the upper left corner (not marked). The sources (of the type h_{zx}) at the lower two corners do not give any wavefield injection onto the FD grids. (d) h_{xz} source injection [compared to Fig. C.16(c, right)]. Source injection at the lower left corner is the same as that at the upper left corner (not marked). The sources (of type h_{xz}) at the right two corners do not give any wavefield injection.

References

- [1] O.E. Aaker, E.B. Raknes, Ø. Pedersen, B. Arntsen, Wavefield reconstruction for velocity-stress elastodynamic full-waveform inversion, *Geophys. J. Int.* 222 (2020) 595–609, <https://doi.org/10.1093/gji/ggaa147>, <https://academic.oup.com/gji/article-pdf/222/1/595/33237700/ggaa147.pdf>.
- [2] K. Aki, P. Richards, *Quantitative Seismology*, University Science Books, 2002.
- [3] A. Akinsunmade, J. Karczewski, E. Mazurkiewicz, S. Tomecka-Suchoń, Finite-difference time domain (FDTD) modeling of ground penetrating radar pulse energy for locating burial sites, *Acta Geophys.* 67 (2019) 1945–1953, <https://doi.org/10.1007/s11600-019-00352-9>.
- [4] G. Arfken, *Mathematical Methods for Physicists*, 3rd ed., Academic Press, Orlando, FL, 1985, https://books.google.ch/books?id=qLfo_Z-PoGIC.
- [5] K. Beach, B. Dunmire, *Medical Acoustics*, Springer, New York, NY, 2007.
- [6] T.S. Becker, N. Börsing, T. Haag, C. Bärlocher, C.M. Donahue, A. Curtis, J.O.A. Robertsson, D.J. van Manen, Real-time immersion of physical experiments in virtual wave-physics domains, *Phys. Rev. Appl.* (2020), <https://doi.org/10.1103/PhysRevApplied.13.064061>.
- [7] T.S. Becker, D.J. van Manen, C.M. Donahue, C. Bärlocher, N. Börsing, F. Broggin, T. Haag, J.O.A. Robertsson, D.R. Schmidt, S.A. Greenhalgh, T.E. Blum, Immersive wave propagation experimentation: physical implementation and one-dimensional acoustic results, *Phys. Rev. X* 8 (2018) 031011, <https://doi.org/10.1103/PhysRevX.8.031011>.
- [8] N. Börsing, T.S. Becker, A. Curtis, D.J. van Manen, T. Haag, J.O. Robertsson, Cloaking and holography experiments using immersive boundary conditions, *Phys. Rev. Appl.* 12 (2019) 024011, <https://doi.org/10.1103/PhysRevApplied.12.024011>, <https://link.aps.org/doi/10.1103/PhysRevApplied.12.024011>.
- [9] F. Broggin, M. Vasmel, J.O.A. Robertsson, D.J. van Manen, Immersive boundary conditions: theory, implementation, and examples, *Geophysics* 82 (2017) T97–T110, <https://doi.org/10.1190/geo2016-0458.1>.
- [10] Y. Duan, A. Guitton, P. Sava, Elastic least-squares reverse time migration, *Geophysics* 82 (2017) S315–S325, <https://doi.org/10.1190/geo2016-0564.1>.
- [11] F. Farias, R. Pestana, Comparing Strategies for Local FWI: FD Injection and Immersive Boundary Conditions, *European Association of Geoscientists & Engineers*, 2020, pp. 1–5.
- [12] A. Fichtner, *Full Seismic Waveform Modelling and Inversion*, Advances in Geophysical and Environmental Mechanics and Mathematics, Springer, Berlin, Heidelberg, 2010, <https://books.google.ch/books?id=wuXvkbQKkwC>.
- [13] J. Fokkema, P. van den Berg, *Seismic Applications of Acoustic Reciprocity*, Elsevier Science, 2013.
- [14] B. Fornberg, Generation of finite difference formulas on arbitrarily spaced grids, *Math. Comput.* 51 (1988) 699–706, <http://www.jstor.org/stable/2008770>.
- [15] D. Givoli, D. Cohen, Nonreflecting boundary conditions based on Kirchhoff-type formulae, *J. Comput. Phys.* 117 (1995) 102–113.
- [16] M. Grote, C. Kirsch, Nonreflecting boundary condition for time-dependent multiple scattering, *J. Comput. Phys.* 221 (2007) 41–62.
- [17] M.J. Grote, J.B. Keller, Nonreflecting boundary conditions for time-dependent scattering, *J. Comput. Phys.* 127 (1996) 52–65.
- [18] M.J. Grote, I. Sim, Local nonreflecting boundary condition for time-dependent multiple scattering, *J. Comput. Phys.* 230 (2011) 3135–3154, <https://doi.org/10.1016/j.jcp.2011.01.017>.
- [19] R.A. Guyer, P.A. Johnson, *Nonlinear Mesoscopic Elasticity: The Complex Behaviour of Rocks, Soil, Concrete*, Wiley, New York, 2009.
- [20] D. Halliday, A. Curtis, An interferometric theory of source-receiver scattering and imaging, *Geophysics* 75 (2010) SA95–SA103, <https://doi.org/10.1190/1.3486453>.
- [21] J. Hartley, A. Giannopoulos, C. Warren, A Huygens subgridding approach for efficient modelling of ground penetrating radar using the finite-difference time-domain method, in: 2018 17th International Conference on Ground Penetrating Radar, GPR, 2018, pp. 1–6.
- [22] L.E. Jaimes-Osorio, A. Malcolm, P. Zheglava, E.F.M. Koene, H.R. Thomsen, Reduced memory implementation of a local elastic finite-difference solver, *Geophysics* 86 (2021) F25–F33, <https://doi.org/10.1190/geo2020-0468.1>.
- [23] E. Koene, J. Robertsson, A finite-difference algorithm to retrieve finite-difference modeled elastic waves at the free surface, 2018, pp. 3923–3927.
- [24] J. Kristek, P. Moczo, R.J. Archuleta, Efficient methods to simulate planar free surface in the 3D 4th-order staggered-grid finite-difference schemes, *Stud. Geophys. Geod.* 46 (2002) 355–381, <https://doi.org/10.1023/A:1019866422821>.
- [25] A. Kyriakou, *Multi-physics computational modeling of focused ultrasound therapies*, Ph.D. thesis, ETH Zurich, Zurich, 2015.
- [26] S. Lambot, E. Slob, I. van den Bosch, B. Stockbroeckx, M. Vanclooster, Modeling of ground-penetrating radar for accurate characterization of subsurface electric properties, *IEEE Trans. Geosci. Remote Sens.* 42 (2004) 2555–2568, <https://doi.org/10.1109/TGRS.2004.834800>.
- [27] X. Li, J. Robertsson, A. Curtis, D.J. van Manen, Compensating for source directivity in immersive wave experimentation, *J. Acoust. Soc. Am.* 146 (2019) 3141–3158, <https://doi.org/10.1121/1.5131029>.
- [28] C. Lin, V. Monteller, K. Wang, T. Liu, P. Tong, Q. Liu, High-frequency seismic wave modelling of the deep Earth based on hybrid methods and spectral-element simulations: a conceptual study, *Geophys. J. Int.* 219 (2019) 1948–1969, <https://doi.org/10.1093/gji/ggz413>.
- [29] D.J. van Manen, *Time-reversal and Interferometry with applications to forward modeling of wave propagation and a chapter on receiver functions*, Ph.D. thesis, University of Edinburgh, 2006.
- [30] D.J. van Manen, X. Li, M. Vasmel, F. Broggin, J. Robertsson, Exact extrapolation and immersive modelling with finite-difference injection, *Geophys. J. Int.* 223 (2020) 584–598, <https://doi.org/10.1093/gji/ggaa317>, <https://academic.oup.com/gji/article-pdf/223/1/584/33549473/ggaa317.pdf>.
- [31] D.J. van Manen, J.O.A. Robertsson, A. Curtis, Exact wave field simulation for finite-volume scattering problems, *J. Acoust. Soc. Am.* 122 (2007) EL115–EL121, <https://doi.org/10.1121/1.2771371>.
- [32] J.L. Mari, M. Mendes, High resolution 3d near surface imaging of fracture corridors and cavities by combining plus-minus method and refraction tomography, *Near Surf. Geophys.* 10 (2012) 185–195, <https://doi.org/10.3997/1873-0604.2011052>, <https://www.earthdoc.org/content/journals/10.3997/1873-0604.2011052>.
- [33] Y. Masson, P. Cupillard, Y. Capdeville, B. Romanowicz, On the numerical implementation of time-reversal mirrors for tomographic imaging, *Geophys. J. Int.* 196 (2013) 1580–1599, <https://doi.org/10.1093/gji/ggt459>, <http://oup.prod.sis.lan/gji/article-pdf/196/3/1580/1557555/ggt459.pdf>.
- [34] Y. Masson, B. Romanowicz, Fast computation of synthetic seismograms within a medium containing remote localized perturbations: a numerical solution to the scattering problem, *Geophys. J. Int.* 208 (2016) 674–692, <https://doi.org/10.1093/gji/ggw412>, <http://arxiv.org/abs/http://oup.prod.sis.lan/gji/article-pdf/208/2/674/8758403/ggw412.pdf>.
- [35] Y. Masson, B. Romanowicz, Box tomography: localized imaging of remote targets buried in an unknown medium, a step forward for understanding key structures in the deep Earth, *Geophys. J. Int.* 211 (2017) 141–163, <https://doi.org/10.1093/gji/ggx141>.
- [36] H. Maurer, A. Curtis, D.E. Boerner, Recent advances in optimized geophysical survey design, *Geophysics* 75 (2010) 75A177–75A194, <https://doi.org/10.1190/1.3484194>.
- [37] R. Mittet, Implementation of the Kirchhoff integral for elastic waves in staggered-grid modeling schemes, *Geophysics* 59 (1994) 1894–1901, <https://doi.org/10.1190/1.1443576>.
- [38] R. Mittet, Free-surface boundary conditions for elastic staggered-grid modeling schemes, *Geophysics* 67 (2002) 1616–1623.
- [39] P. Moczo, J.O. Robertsson, L. Eisner, The finite-difference time-domain method for modeling of seismic wave propagation, in: R.S. Wu, V. Maupin, R. Dmowska (Eds.), *Advances in Wave Propagation in Heterogeneous Earth*, in: *Advances in Geophysics*, vol. 48, Elsevier, 2007, pp. 421–516.
- [40] I.L.C. Ning, P. Sava, *Seismic imaging with optimal source wavefield reconstruction*, in: *SEG Technical Program Expanded Abstracts*, 2019, pp. 4156–4160.
- [41] N. Nosjean, Y. Khamitov, S. Rodriguez, R. Yahia-Cherif, Fracture corridor identification through 3d multifocusing to improve well deliverability, an Algerian tight reservoir case study, *Solid Earth Sci.* 5 (2020) 31–49, <https://doi.org/10.1016/j.sesci.2019.11.009>, <https://www.sciencedirect.com/science/article/pii/S2451912X19300455>.

- [42] M. Pienkowska, V. Monteiller, T. Nissen-Meyer, High-frequency global wavefields for local 3D structures by wavefield injection and extrapolation, *Geophys. J. Int.* (2020), <https://doi.org/10.1093/gji/ggaa563>, <https://academic.oup.com/gji/advance-article-pdf/doi/10.1093/gji/ggaa563/34484085/ggaa563.pdf>.
- [43] M. Ravasi, A. Curtis, Elastic imaging with exact wavefield extrapolation for application to ocean-bottom 4C seismic data, *Geophysics* 78 (2013) S265–S284, <https://doi.org/10.1190/geo2013-0152.1>.
- [44] J.L.B. Robertson, B.T. Cox, J. Jaros, B.E. Treeby, Accurate simulation of transcranial ultrasound propagation for ultrasonic neuromodulation and stimulation, *J. Acoust. Soc. Am.* 141 (2017) 1726–1738, <https://doi.org/10.1121/1.4976339>.
- [45] J.O. Robertsson, D.J. van Manen, C. Schmelzbach, C. Van Renterghem, L. Amundsen, Finite-difference modelling of wavefield constituents, *Geophys. J. Int.* 203 (2015) 1334–1342, <https://doi.org/10.1093/gji/ggv379>, <http://oup.prod.sis.lan/gji/article-pdf/203/2/1334/5880849/ggv379.pdf>.
- [46] J.O.A. Robertsson, A numerical free-surface condition for elastic/viscoelastic finite-difference modeling in the presence of topography, *Geophysics* 61 (1996) 1921–1934.
- [47] J.O.A. Robertsson, C.H. Chapman, An efficient method for calculating finite-difference seismograms after model alterations, *Geophysics* 65 (2000) 907–918, <https://doi.org/10.1190/1.1444787>.
- [48] J.A. Roden, S.D. Gedney, Convolution PML (CPML): an efficient FDTD implementation of the CFS-PML for arbitrary media, *Microw. Opt. Technol. Lett.* 27 (2000) 334–339, [https://doi.org/10.1002/1098-2760\(20001205\)27:5<334::AID-MOP14>3.0.CO;2-A](https://doi.org/10.1002/1098-2760(20001205)27:5<334::AID-MOP14>3.0.CO;2-A).
- [49] P. Routh, G. Palacharla, I. Chikichev, S. Lazaratos, Full wavefield inversion of time-lapse data for improved imaging and reservoir characterization, in: *SEG Technical Program Expanded Abstracts*, 2012, pp. 1–6.
- [50] V. Ryabenkii, S. Tsynkov, V. Turchaninov, Global discrete artificial boundary conditions for time-dependent wave propagation, *J. Comput. Phys.* 174 (2001) 712–758.
- [51] G.T. Schuster, A hybrid BIE+Born series modeling scheme: generalized Born series, *J. Acoust. Soc. Am.* 77 (1985) 865–879.
- [52] J. Singh, A. Mulholland, K. Tant, T. Stratoudaki, A. Curtis, W. Ijomah, J. Windmill, Component shape optimisation for enhanced non-destructive testing, *Mater. Des.* 195 (2020) 109041, <https://doi.org/10.1016/j.matdes.2020.109041>, <https://www.sciencedirect.com/science/article/pii/S0264127520305761>.
- [53] R. Snieder, Chapter 1.7.1 - General theory of elastic wave scattering, in: R. Pike, P. Sabatier (Eds.), *Scattering*, Academic Press, London, 2002, pp. 528–542, <http://www.sciencedirect.com/science/article/pii/B9780126137606500279>.
- [54] M. Solovchuk, T.W.H. Sheu, M. Thiriet, Multiphysics modeling of liver tumor ablation by high intensity focused ultrasound, *Commun. Comput. Phys.* 18 (2015) 1050–1071, <https://doi.org/10.4208/cicp.171214.200715c>.
- [55] A. Tarantola, Inversion of seismic reflection data in the acoustic approximation, *Geophysics* 49 (1984) 1259–1266, <https://doi.org/10.1190/1.1441754>.
- [56] Z.H. Teng, Exact boundary condition for time-dependent wave equation based on boundary integral, *J. Comput. Phys.* 190 (2003) 398–418, [https://doi.org/10.1016/S0021-9991\(03\)00281-X](https://doi.org/10.1016/S0021-9991(03)00281-X).
- [57] H.R. Thomsen, E.F.M. Koene, J.O.A. Robertsson, D.-J. van Manen, FD-injection-based elastic wavefield separation for open and closed configurations, *Geophys. J. Int.* 227 (3) (2021) 1646–1664, <https://doi.org/10.1093/gji/ggab275>.
- [58] H.R. Thomsen, D.J. van Manen, J. Robertsson, Exact wavefield separation on an elastic free surface with sharp corners, in: *SEG International Exposition and 88th Annual Meeting*, 2018, pp. 5017–5021.
- [59] H.R. Thomsen, M. Molerón, T. Haag, D.J. van Manen, J.O.A. Robertsson, Elastic immersive wave experimentation: theory and physical implementation, *Phys. Rev. Res.* 1 (2019) 033203, <https://doi.org/10.1103/PhysRevResearch.1.033203>.
- [60] C.J. Thomson, Research note: internal/external seismic source wavefield separation and cancellation, *Geophys. Prospect.* 60 (2012) 581–587, <https://doi.org/10.1111/j.1365-2478.2011.01043.x>.
- [61] L. Ting, M. Miksis, Exact boundary conditions for scattering problems, *J. Acoust. Soc. Am.* 80 (1986) 1825–1827, <https://doi.org/10.1121/1.394297>.
- [62] I. Vasconcelos, R. Snieder, H. Douma, Representation theorems and Green's function retrieval for scattering in acoustic media, *Phys. Rev. E* 80 (2009) 036605, <https://doi.org/10.1103/PhysRevE.80.036605>, <https://link.aps.org/doi/10.1103/PhysRevE.80.036605>.
- [63] M. Vasmel, J.O.A. Robertsson, Exact wavefield reconstruction on finite-difference grids with minimal memory requirements, *Geophysics* 81 (2016) T303–T309, <https://doi.org/10.1190/geo2016-0060.1>.
- [64] M. Vasmel, J.O.A. Robertsson, D.J. van Manen, A. Curtis, Immersive experimentation in a wave propagation laboratory, *J. Acoust. Soc. Am.* 134 (2013) EL492–EL498, <https://doi.org/10.1121/1.4826912>.
- [65] J. Virieux, P-SV wave propagation in heterogeneous media: velocity-stress finite-difference method, *Geophysics* 51 (1986) 889–901, <https://doi.org/10.1190/1.1442147>.
- [66] T.S. Becker, D.-J. van Manen, T. Haag, C. Bärlocher, X. Li, N. Börsing, A. Curtis, M. Serra-García, J.O.A. Robertsson, Broadband acoustic invisibility and illusions, *Sci. Adv.* 7 (37) (2021) eabi9627, <https://doi.org/10.1126/sciadv.abi9627>.
- [67] J. Virieux, S. Operto, An overview of full-waveform inversion in exploration geophysics, *Geophysics* 74 (2009) WCC1–WCC26, <https://doi.org/10.1190/1.3238367>.
- [68] B. Wang, S. Zhong, T.L. Lee, K.S. Fancy, J. Mi, Non-destructive testing and evaluation of composite materials/structures: a state-of-the-art review, *Adv. Mech. Eng.* 12 (2020) 1687814020913761, <https://doi.org/10.1177/1687814020913761>.
- [69] Y. Wang, Frequencies of the Ricker wavelet, *Geophysics* 80 (2015) A31–A37, <https://doi.org/10.1190/geo2014-0441.1>.
- [70] K. Wapenaar, J. Fokkema, Green's function representations for seismic interferometry, *Geophysics* 71 (2006) SI33–SI46, <https://doi.org/10.1190/1.2213955>.
- [71] H. Wiggenhauser, C. Köpp, J. Timofeev, H. Azari, Controlled creating of cracks in concrete for non-destructive testing, *J. Nondestruct. Eval.* 37 (2018) 67, <https://doi.org/10.1007/s10921-018-0517-x>.
- [72] B. Willemssen, A. Malcolm, W. Lewis, A numerically exact local solver applied to salt boundary inversion in seismic full-waveform inversion, *Geophys. J. Int.* 204 (2016) 1703–1720, <https://doi.org/10.1093/gji/ggv547>.
- [73] U. Zerbst, T. Heckel, M. Carboni, Non-destructive testing and fracture mechanics: a short discussion, *AIP Conf. Proc.* 1706 (2016) 150002, <https://doi.org/10.1063/1.4940614>.